Msc Thesis

Solid oxide fuel cell electrolyte: The synthesis and X-ray diffraction refinement of the $Ba_3MoNb_{1-x}V_xO_{8.5}$ series

Author: Frederik Floyd Beuzenberg, 4455231
Academic year 2023-2024

Supervisors:
Dr. Pedro Braga Groszewicz
Abdulkadir Olatunbosun Biffo
Dr. Amarante J. Böttger

TU Delft

Abstract.
The $Ba_3MoNb_{1-x}V_xO_{8.5}$ family exhibits significant oxide ion conductivity, and is thus interesting in the potential use of solid oxide fuel cells as an electrolyte. Its structure contains palmierite-like layers consisting of metallic cations forming octahedral and tetrahedral polyhedra, through which the oxide ions can be conducted. Furthermore, the cationic vacancies present in the structure lead to complex stacking configurations beneficial to the conductivity. In this work the $Ba_3MoNb_{1-x}V_xO_{8.5}$ family, with x = 0.0, 0.1, 0.2, 0.3, 0.4, have been synthesised and analysed with the use of X-ray diffraction and subsequent refinement of their structures. The synthesis for each sample was performed successfully, and the first calcination step was further identified to bring a higher yield under higher temperature and longer time of the calcination. From the LeBail refinement the *a* lattice parameter was shown to correlate with Vegard's law, decreasing with an increase of substitution of Nb^{5+} with V^{5+}, whilst the *c* parameter expands upon substitution of the smaller cation. This is hypothesised to be caused by repulsion, either coming from distortions caused by second-order Jahn Teller effect, or due to more tetrahedral coordination. Finally, the Rietveld refinement has given insight into the location and occupation of the metallic cations. V^{5+} has been incorporated into the solid solution, and sits on the same crystallographic sites as the other metallic cations, choosing to split off to either one of the two sites, thereby contradicting earlier literature. Furthermore, the vanadium doping also seems to move the overall concentration of Mo^{6+} and Nb^{5+} to one site in particular. These results have thereby given new insight into this family of solid electrolytes.

Content.

1. Introduction.

Since the start of the industrial era humanity has begun using different forms of energy, such as steam power and electricity to power their machinery and devices. These forms of energy were, and still are in large quantities, generated by fossil fuels, like natural gas, oil, and coal. However, these sources of energy are limited and will likely run out in the coming century, are generally used in inefficient manners, wasting part of their potential energy, and above all severely polluting our climate, giving rise to global warming and climate change. Thus humanity has been assigned the task to find alternative methods of generating energy; methods that will not be gravely limited in their abundance, that will use their fuels to their highest potential and mitigate their impact on our environment. The world is moving in such directions, with the advancements in generating power from solar, wind, and nuclear energy.

Generally, energy generated in this way is captured as electricity, which needs to either be used directly or be stored in some capacity. Whilst usage throughout a network is possible for many applications, the large increase in electricity generated from sources like solar power does bring a lot of strain on such a network. For other applications, such as vehicles, as well as to alleviate the strain on the network, storage of this power would be beneficial. Generally, this power is stored as electricity, but the problem with such storage is often the large volumetric size required for storing energy in this way. A more sizable method of energy storage would be within hydrogen bonds in the form of H_2, which can be created through electrochemical conversion.

This is where the solid oxide fuel cells (SOFCs) come in. SOFCs are part of the solid oxide cells group, which can generally be separated into two categories, namely solid oxide electrolyser cells (SOECs) and SOFCs. [1] The former is used to convert electrical power into hydrogen, allowing for alternate storage options and alleviating the stress from the power grid, whilst the latter can be used to generate electrical power from various fuels in a relatively clean and efficient manner, through the use of electrochemical reactions. The SOFC cell consists of a solid ceramic electrolyte with the ability to conduct ions in between two porous electrodes, without the diffusion of electrons, as that would limit their efficiency. A schematic diagram in figure 1 shows the parts of the SOFC, as well as the manner in which fuel is converted into electricity. The ideal fuel for a SOFC would be hydrogen, in that it has a high gravimetric energy density and does not create any problems regarding degradation of the cell, as opposed to alternative fuels, like hydrocarbons, alcohols, or ammonia. [2] However, the latter are more commercially available, thus a SOFC should also preferably also be able to adapt to these fuel sources. Furthermore, to have a solid electrolyte be commercially available, it must adhere to a few requirements [3]:

- A sufficiently high oxide conductivity (0.01 - 0.1 S/cm)
- A low electronic transference number ($< 10^{-3}$)
- Thermodynamic and chemical stability from room to operating temperature and a large range of oxygen partial pressures
- Both chemical inertness as well as compatible thermal expansion coefficient with the electrodes
- Able to withstand a sizeable amount of mechanical stress

A number of electrolytes that adhere to or come close to meeting these requirements have been commercialised. The most common one is yttria-stabilised zirconia (YSZ), and its derivative scandium-stabilised zirconia (ScSZ), with the latter having a slightly higher ionic conductivity. Both crystallise into cubic fluorite structures, which conduct oxide ions through

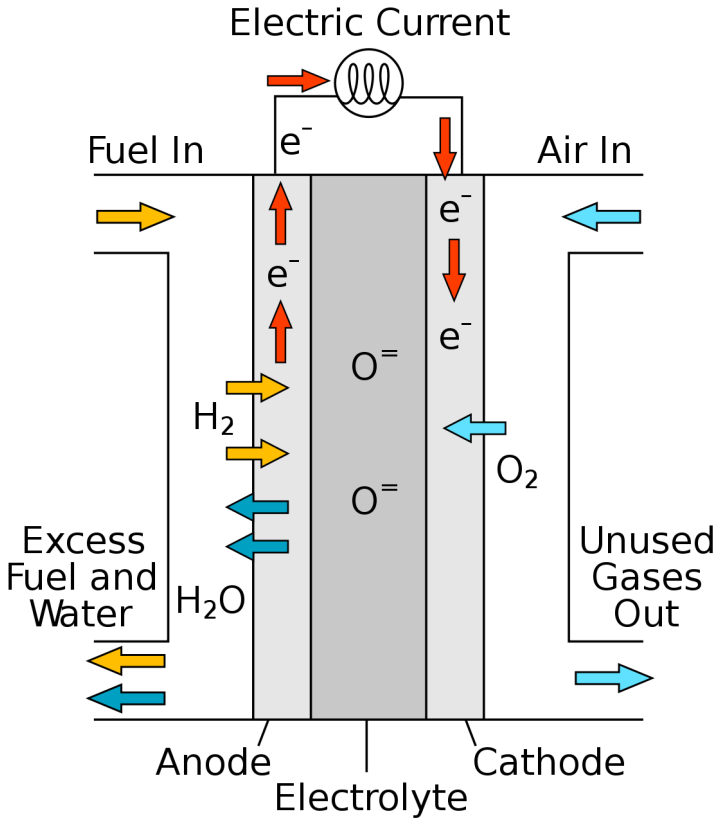

Figure 1. Schematic representation of a solid-oxide fuel cell, with fuel entering from the left and oxygen and entering from the right, which travels through the solid electrolyte to generate electricity and react at the anode [6]

vacancies introduced by acceptor doping. [4,5] Another favourite is gadolinium-doped ceria (Gd:CeO_2, GDC), having the same fluorite crystal structure and means of oxide ion conduction as the YSZ derivatives, but outperforming them in actual conductivity. However, gadolinium is a rather sparse material and both the mechanical and chemical stability of the structure are inferior to YSZ, thereby generally manufacturers giving preference to use of the latter. [7]

Apart from the requirements stated above, one of the current challenges in the deployment of SOFCs is the operating temperature of 700 °C or higher, required for ionic conduction through the ceramic oxide ion conductor to facilitate the electrochemical reactions occurring at the interface with the electrodes. The high operating temperature is detrimental in the sense of the high system and maintenance costs, degradation of the performance leading to poor durability, slow start-up and shutdown times, and finding compatible materials functioning at such high temperatures. [8] Thus to overcome these limitations, electrolyte materials having satisfactory ionic conductivity at intermediate or lower temperatures (<500 °C) are being sought after. This has led to the exploration of a wide variety of structural families with proven oxide ion conductivity.

One such family is the LAMOX family, with its oxide ion conductivity first studied by Lacorre et al. in the year 2000. [9] The base compound is $La_2Mo_2O_9$, in which the lanthanum site is doped by dysprosium, and the molybdenum site with atoms such as tungsten, vanadium, gallium, and chromium. So far their oxide ion conductivity has reached the range of 10^{-2} - 10^{-1} S cm^{-1} at 800 °C. [10] Another family is the ‘bismuth metal vanadium oxide’ (BIMEVOX)

family, which was first studied in 1990 by Abraham et al. [11] It has the general formula $Bi_4V_2O_{11}$ and belongs to the Aurivillius structural family. Oxide ions within this structure diffuse along the oxygen deficient vanadium-oxygen layer, attributing to its fast oxide conductivity. Through doping the vanadium site with copper, a conductivity of 0.1 - 0.2 S cm^{-1} at 600 °C can be reached. [12] In 1994, Ishihara et al., and Feng and Goodenough doped $LaGaO_3$ with strontium and magnesium to create $La_{1-x}Sr_xGa_{1-y}Mg_yO_3$, or what is now better known as LSGM. [13,14] The crystal structure has been debated, with some reports of cubic and monoclinic systems, but the oxide ion conductivity is generally best at doping levels around 0.2 for both *x* and *y*, resulting in conductivities around 0.1 S cm^{-1} at 800 °C. [15]
Each of these electrolytic compounds have a different structural family, but the one that caught the interest of this study has been the hexagonal perovskite family. The field of oxide ion conduction in this family is rather new, with one of the earlier works having been produced by Kuang et al. [16] in which they synthesised $Ba_7Y_2Mn_3Ti_4O_{20}$. For this structure the bulk conductivity was measured to be around 2.6 * 10^{-3} S cm^{-1} at 700 °C, thereby showing that hexagonal perovskites could potentially be good oxide-ion conductors. The capability of hexagonal perovskites for conduction comes from their structure, which is based on, as the name implies, on the common perovskite structure. The common perovskite has the ABX_3 formula, with X usually being occupied by oxygen. The ideal cubic perovskites consist of octahedra sharing corners, as seen in figure 4a in chapter 2, but, as will be explained in more detail in chapter 2, in non-ideal circumstances these face-sharing is also possible. Through stacking of corner-sharing (cubic) and face-sharing (hexagonal) layers, different superstructures can be formed. To illustrate, $BaRuO_3$ has been studied by Kanungo et al., in which they altered the production method by increasing the pressure, creating different stacked structures, as can be seen in figure 2. [17] In this case, with an increase in pressure the structure adapts to have a decreasing amount of hexagonal layers. Each of these compounds showed different electronic, magnetic, and optical properties, thus

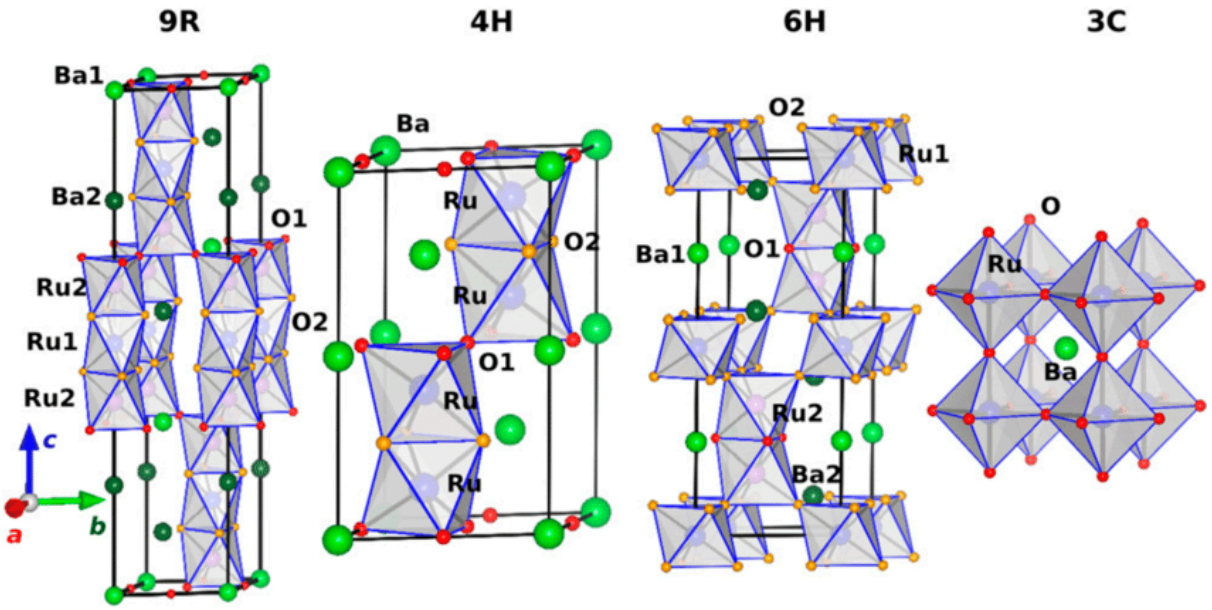

Figure 2. Examples of the multitude of structures the compound $BaRuO_3$ can form into under applied pressure. [17]

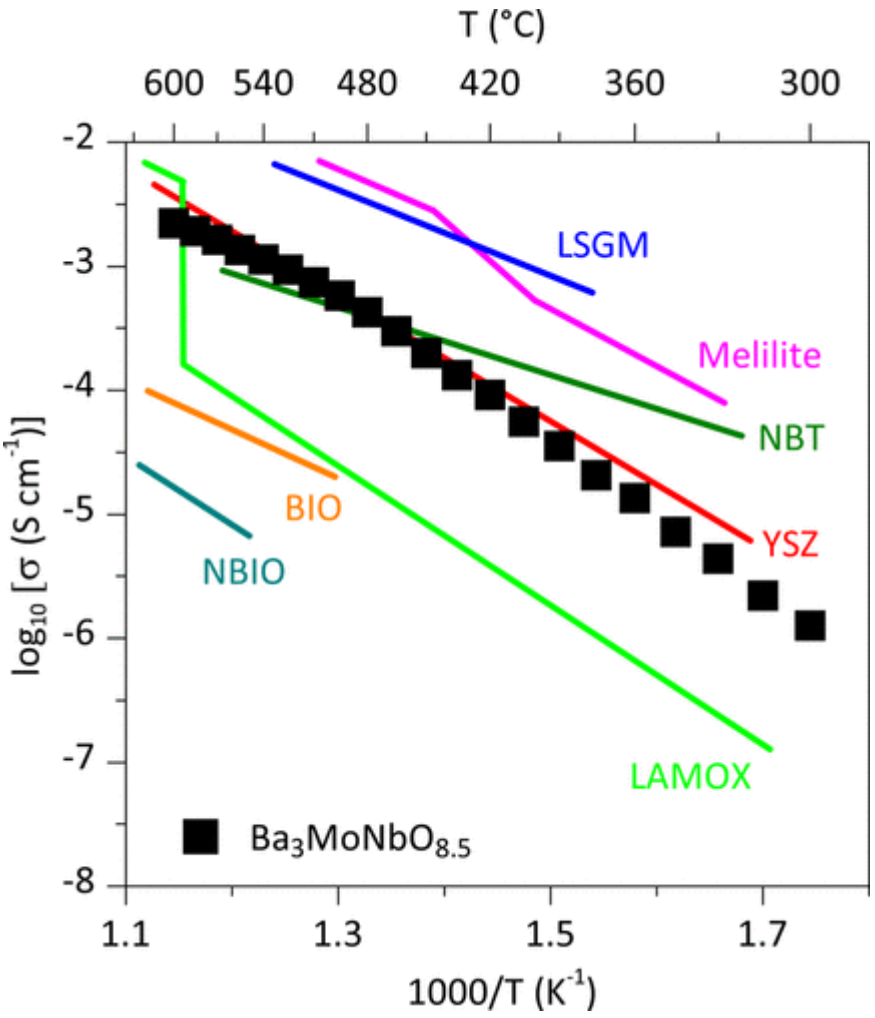

Figure 3. Comparison of bulk conductivities of $Ba_3MoNbO_{8.5}$ and other commonly researched ionic conductors. [18]

evidencing that the structure plays a vital part in these properties.

In terms of oxide ion conductivity in hexagonal perovskites, the $Ba_3M'M''O_{8.5\pm\square}$ family has garnered much attention, when Fop et al. first studied the oxide ion conductivity of $Ba_3MoNbO_{8.5}$ [18]. Like $BaRuO_3$, it has a stacking sequence of $(hhc)_3$ similar to the 9R polytype seen in figure 2, in which the barium atoms form the framework and the other metallic cations occupy the centres of the octahedra. However, in this case it does not have an equal amount of A and B atoms, leading to a cationic deficiency and filling two thirds of each trimer. On the other hand, the palmierite structure (as shown on the right in figure 3) has the $A_3B_2O_8$ structure, with the cationic deficiency being organised on the centre of each trimer. To maintain charge neutrality, this structure also misses one oxygen, causing a reorganisation from octahedral to tetrahedral coordination on the ends of the trimers. [18] $Ba_3MoNbO_{8.5}$ is an interesting case in which it seems to adapt a hybrid between the two, with a more variable occupation of the trimer as opposed to palmierite, but with the option for the ends of the trimer to adapt either octahedral or tetrahedral coordination. From their original paper, the bulk conductivity for oxide ions was determined to be $2.2 * 10^{-3}$ S cm^{-1} at 600 °C. Thereby it was already competitive with the commonly used YSZ electrolyte (as can be seen in figure 3), with still room for improvement. [18]

From further research, the general consensus developed that with more tetrahedral coordination, the oxide ion conductivity improves. Since the discovery of Fop et al., his team and many others have begun researching derivatives of this structural family by doping or replacing the metallic cations. So far there have been attempts at synthesising the following derivative structures, with varying amounts of success: $Ba_3Mo_{1-x}Nb_{1+x}O_{8.5-x/2}$ [19], $Ba_3WNbO_{8.5}$ [20,21], $Ba_3MoV_xNb_{1-x}O_{8.5}$ [22], $Ba_3WVO_{8.5}$ [23,24], $Ba_3W_{1+x}V_{1-x}O_{8.5+x/2}$ [25], and $Ba_3MoVO_{8.5}$ [26]. These studies only use aliovalent doping or doping with elements from groups V and VI on the periodic table. The highest achieved bulk oxide ion conductivity for this group was achieved by $Ba_3MoNb_{0.9}V_{0.1}O_{8.5}$, with 1.0 * 10^{-2} S cm^{-1} at 600 °C. From these studies the following trends were gathered:

- Between Mo^{6+} and Nb^{5+}, Mo^{6+} has a slightly higher preference for tetrahedral coordination.
- W^{6+} prefers octahedral coordination, thereby decreasing the oxide ion conductivity, but may mitigate the Jahn-Teller distortion of the structure, which increases conductivity.
- V^{5+} prefers tetrahedral coordination, thereby increasing the oxide ion conductivity, but causes heavy Jahn-Teller distortion,thereby limiting its positive effect.
- Aliovalent doping by which the amount of oxygen in the structure increases, increases the oxide ion conductivity.

Whilst these trends are evidenced, the exact workings behind them on an atomic level are yet to be disclosed. The focus of this thesis was drawn towards V^{5+}, in particular the $Ba_3MoNb_{1-x}V_xO_{8.5}$ compounds, because of discrepancies found in the work of Fop et al. in 2020. [22] As stated, for x = 0.1, they have achieved the highest oxide ion conductivity, but this achievement has only been recorded once. Furthermore, their Rietveld refinement of their NPD and XRD data shows a relatively high occupancy for V^{5+} on the central site of the trimer. This site is exclusively octahedrally coordinated, which raises the question on why V^{5+}, which was assumed to have a high preference for tetrahedral coordination, has a relatively high occupancy on this site when compared to Mo^{6+} and V^{5+}. Taking $Ba_3MoNb_{0.9}V_{0.1}O_{8.5}$ as an example, the M1 site, which can coordinate either octahedrally or tetrahedrally, takes about 60% of the V^{5+}, with the rest going towards the M2 site, that coordinates exclusively octahedrally. Comparing this to Nb^{5+}, which has been stated to prefer octahedral coordination more than V^{5+}, 91% sits on the variable M1 site. This trend also does not change with the addition of more vanadium, as even at x = 0.4 the Nb^{5+} has a much higher preferential occupation on the M1 site (95%) than the M2 site, as opposed to V^{5+}, which, although also showing an overall preference for the M1 site, seems less frequently occupying it, with 82.5% of its total residing at it. These results have been left unexplained, leaving us to question what effects the metal cations exactly have on each other's occupational and coordination environment preferences, especially in the case of V^{5+}. Thus this thesis efforts have been made to investigate and explain this discrepancy, by replicating the research

In the following chapter the theory behind the perovskite crystal structure of the material and the methods employed shall be presented. Subsequently, the methodology of the experiments performed shall be elaborated on for any to reproduce. The results gathered from these experiments will be discussed, after which conclusions are presented and an outlook is given on where this research can be taken next.

2. Theory.

2.1. Crystal Structure.

In this thesis the crystal structure of the $Ba_3MoNbO_{8.5}$ family will be extensively discussed, and therefore knowledge on how it is derived from the ideal perovskite structure is most beneficial. The common perovskite has a ABX_3 stoichiometry, with A and B being cations, with A being larger and taking the corner sites and B being smaller and taking the centre site of its cubic structure and X being the anion on the facial positions (see figure 4a). The anions are usually oxygen ions, leading to a -6 charge, which requires compensation from the cations to form an electronically stable structure. The most common manner this is done is by a +4 and a +2 cation ($A^{+4}B^{+2}O^{-2}_3$), but combinations of a +3 with another +3 cation ($A^{+3}B^{+3}O^{-2}_3$), and a +5 with a +1 cation ($A^{+5}B^{+1}O^{-2}_3$) also exist. [27] Perovskite belongs to the $Pm\bar{3}m$ space group, giving the B cations 6-fold octahedral coordination and the A cation 12-fold cuboctahedral coordination with the anions. The octahedron formed out of B-O bonds is rather flexible and can tilt in each of the three directions, leading to 22 different space groups with less symmetry. [28] The level of symmetry, and therefore the space group of the material, can be influenced by changes in temperature, such as $LaGaO_3$ (LSGM) compounds that transform from orthorhombic ($Pbnm$) to rhombohedral ($R\bar{3}c$) at around 150 °C. [29]

In the ideal cubic perovskites all the octahedra only share their corners, and although tilting may occur to form orthorhombic symmetries, the octahedra remain corner-sharing. In hexagonal perovskites this rule is broken, and neighbouring octahedra start sharing faces. This occurs as a consequence of the structural distortion of the perovskite due to the size relationship of the A and B cations. The size relationship can be described by the Goldschmidt tolerance factor, *t*, which is given by:

$$t = \frac{r_A + r_O}{\sqrt{2}(r_B + r_O)} \quad (1)$$

In the ideal cubic situation $0.9 < t < 1$, meaning that the ionic radii cause little distortion, as in $SrTiO_3$. If the ionic radius of B becomes much larger, symmetry will be lost due to distortion and the tolerance factor will be under 0.9, giving orthorhombic symmetry as in $CaTiO_3$, or even different structures, like trigonal in $FeTiO_3$, if the ionic radii become similar. This is due to the octahedra trying to fill up the vacant space left by the relatively small A cation by tilting. On the other hand, when the A cation becomes much larger, the tolerance factor will go above 1, leading to hexagonal or tetrahedral symmetry. In the case of hexagonal systems, the octahedra share faces to release strain caused by the mismatch of the ionic radii. As can be seen in figure 4, the hexagonal structure can be aptly described by the AO_3 layers in the $1\bar{1}1$ plane of the cubic structure, forming the planes perpendicular to the z direction in the hexagonal structure. Situated in the octahedral cavities of these planes are the B cations.

Looking at figure 4b and below, these AO_3 planes can be stacked in either a cubic (c) manner by means of corner sharing or a hexagonal (h) manner by face sharing. For instance, taking a look at $BaRuO_3$, there are a number of different stacking orders that can be created by altering the production methods.

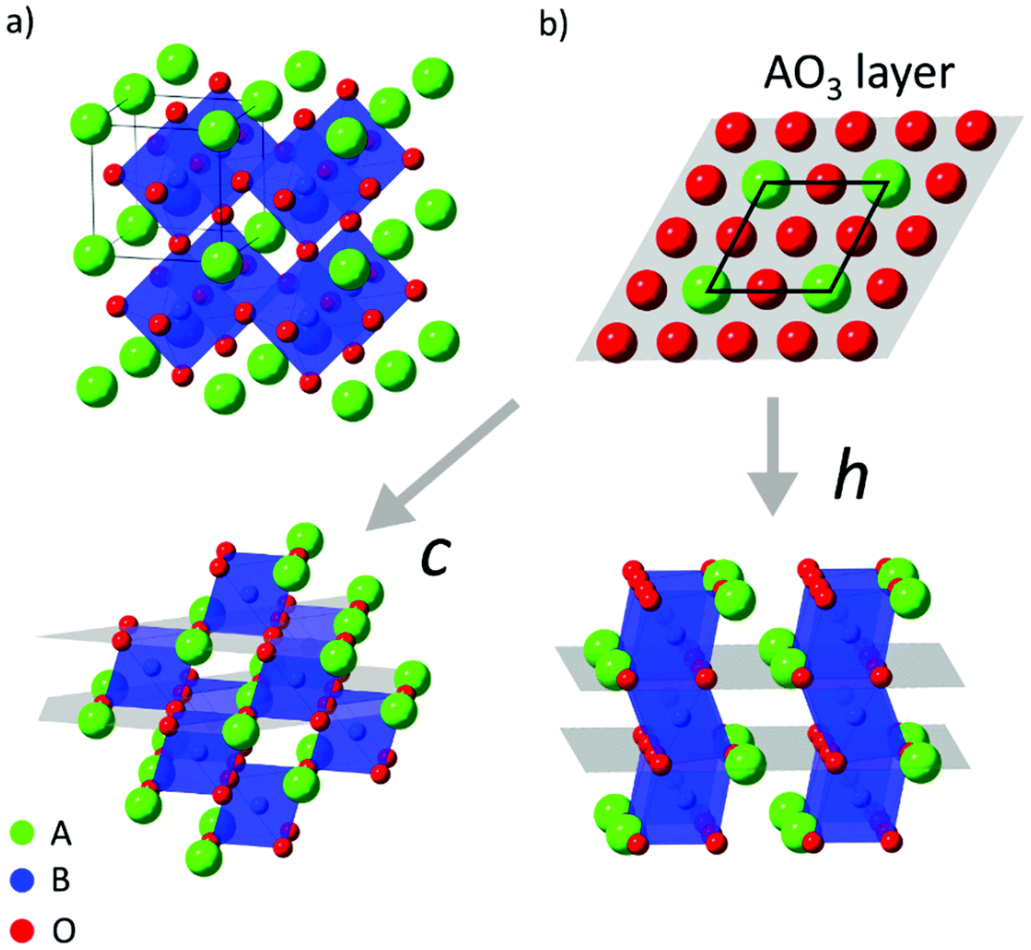

Figure 4. The formation of cubic and hexagonal layers within perovskites due to distortions caused by the size of the cations. [30]

Kanungo et al. have shown using DFT that under varying pressures different perovskite structures form. [17] Under ambient pressure the perovskite structure forms into its 9R structural type, which has a stacking sequence of $(chh)_3$. Figure 2 in chapter 1 shows this stacking sequence, as well as the ones mentioned in the rest of this paragraph, with the red dots of the cubic layer sharing their corners and the yellow dots of the hexagonal layer sharing their faces. Increasing the pressure to 3 GPa leads to the formation of the 4H structural type with a ch_2 stacking sequence, and further increase leads to the 6H polymorph with a $(hcc)_2$ stacking. Finally, further increasing the pressure, leads to the 3C structure, forming the ideal perovskite structure. From the figure and stacking sequences, it can be gathered that the percentage of corner sharing increases as the pressure increases. In their research they investigated the electronic, magnetic, and optical properties of these crystals, finding different properties depending on the structure.

As stated before, $Ba_3MoNbO_{8.5}$ forms into one such hexagonal perovskite structure, quite similar to the 9R structure of $BaRuO_3$ under ambient pressure in figure 2. The 9R polytype is again shown in figure 5, and would belong to a compound with the stoichiometric formula of $Ba_3M_2O_9$, with M being a metallic cation with a 6+ charge. It consists of a framework of Ba^{2+} ions, as shown in the figure in green, essentially creating three stacks of (*chh*) stacked BaO_3

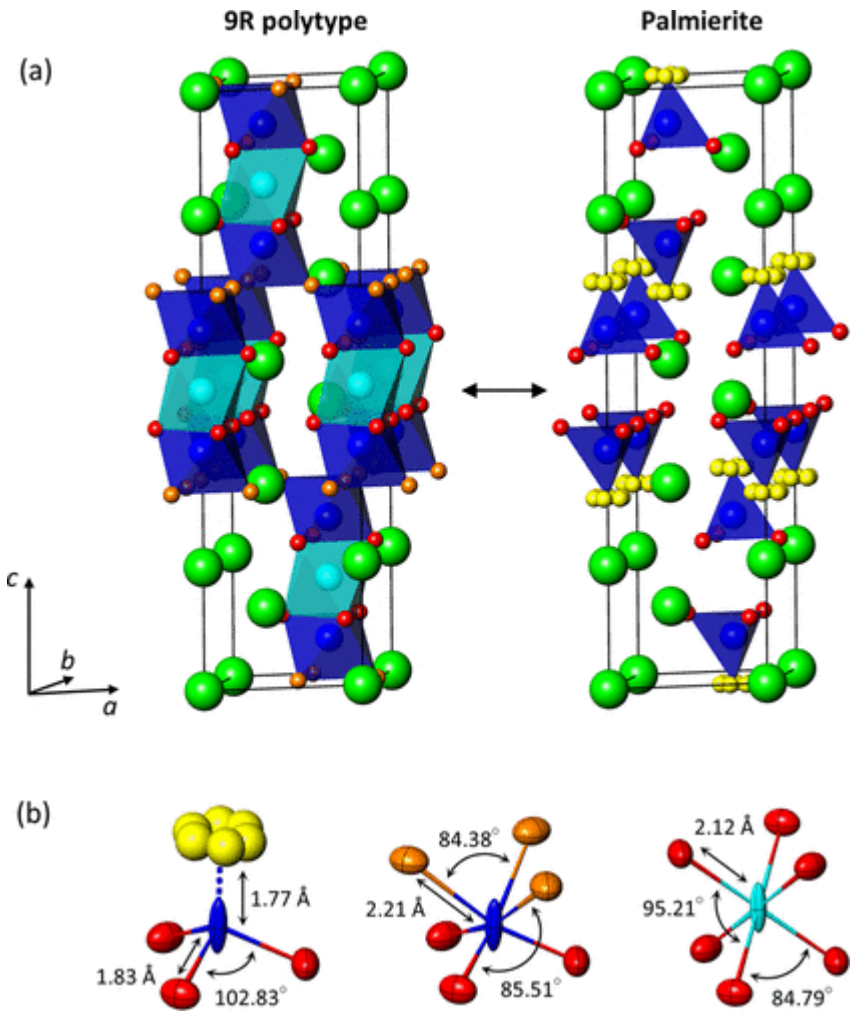

Figure 5. (a) The crystal structures of the 9R polytype and palmierite, forming the hybrid structure, with Ba^{2+} in green, the M1 site in dark blue, the M2 site in cyan, the O1 site in red, the O2 site in orange, and the O3 site in yellow (b) The three different coordination environments found within the hybrid structure. [18]

on top of each other. Filling the gaps are three sets of face-sharing octahedral trimers, containing the metallic cation at their centre, which coordinate with O^{2-} ions to form the octahedra. The trimers are connected to each other through corner-sharing (the orange oxygen atoms), with the dark blue octahedra being the slightly compressed M1 site and the light blue ones the slightly elongated M2 site, compared to the ideal octahedron. On average, each trimer is filled by two metallic cations, thus leaving space for different arrangements within each trimer and giving the structure as a whole a random arrangement. By making the charge of the metallic cations equal to +5, one oxygen atom needs to be removed from the formula, leading to a $Ba_3M_2O_8$ structure better known as palmierite. Whilst the Ba^{2+} network remains the same, as well as the red oxygen positions, the further lack of oxygen causes the cubic BaO_3 layers to rearrange to BaO_2 layers. This in turn forces the M1 site to adopt tetrahedral coordination, and leaves the M2 site completely vacant, leading to a well-organised structure [18].

However, by choosing the metallic cations to be a +6 and a +5 charged one in equal ratio, such as Mo^{6+} and Nb^{5+}, the formula has to maintain charge balance by forming $Ba_3MoNbO_{8.5}$. Its structure will be a hybrid between the 9R polytype and the palmierite structure; the cubic layers will on average contain 2.5 oxygen atoms, thereby giving the

adjacent metallic cations on the M1 sites the option to either form octahedral or tetrahedral coordination. The M2 site can also be occupied, as opposed to palmierite, but can still exclusively coordinate octahedrally. Like the 9R polytype, the two metallic cations per trimer give rise to partial occupation of the sites and lead to a random arrangement of cationic vacancies within the structure [18].

The main reason for investigating this compound in recent years has been in relation to the oxide ion conductivity, and therefore the mechanisms of oxide ion mobility and its dynamics within the structure are rather important. In the $Ba_3MoNbO_{8.5}$ hybrid structure, there are two oxide pathways, the main one along the palmierite layer, and an additional one along the *c*-direction, as shown in figure 6. The pathway along the *c*-direction is of less importance, but derivatives that were evidenced to have no connection along this direction have been shown to have a lower oxide ion conductivity. The main conductive pathway follows an oxygen hopping mechanism through the $BaO_{2.5}$ layer by interchanging the coordination environment with the metallic cations; as demonstrated in the bond-valence site energy (BVSE) map at the bottom of figure 6, the pathway curves around the Ba^{2+} ions, through oxide ion exchange along the connections created between the O2 and O3 sites, and is thus influenced by the distribution of oxygen on these sites. A higher percentage on O3 site occupation, and thus a higher amount of tetrahedral coordination, lowers the relative energy barrier for the saddle point (S1). The second saddle point (S2) is associated with the sinusoidal distribution of the

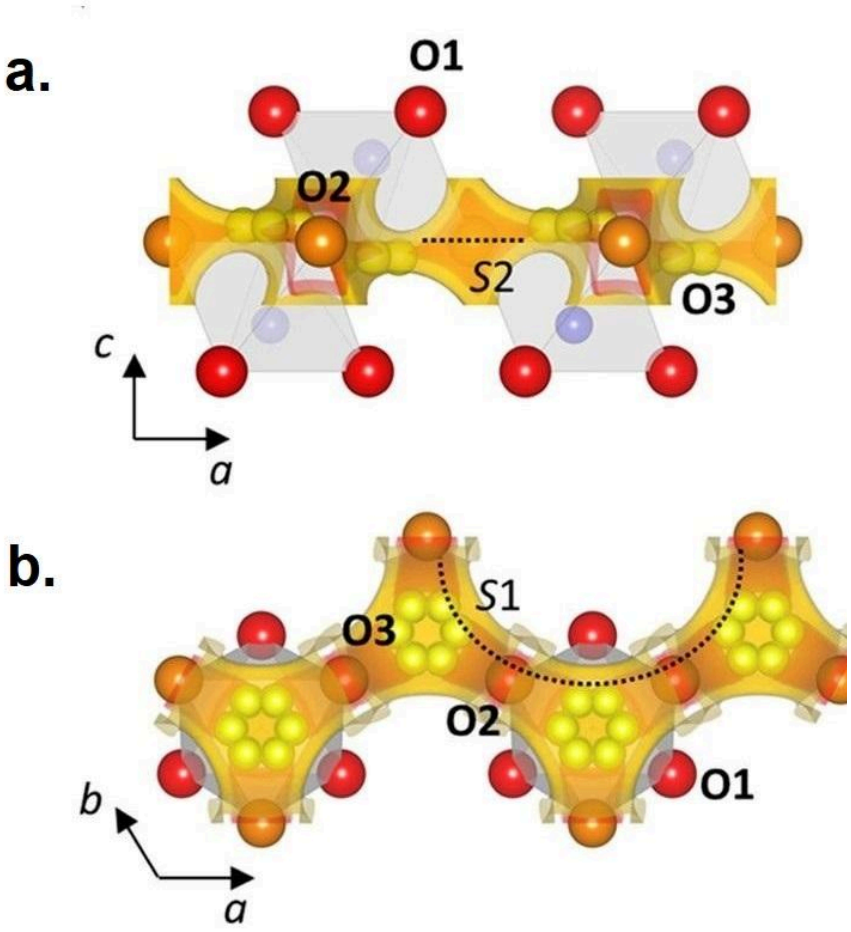

Figure 6. BVSE map showing the oxide ion conductive pathway along the $BaO_{2.5}$ palmierite layer as seen along the b-axis (a.) and the c-axis (b.). [22]

crystallographic sites and the required relaxation for the metal polyhedra during oxygen exchange. The more distorted the polyhedra are, for instance due to second-order Jahn Teller distortions [31], the higher the relative energy barrier will be. Thus the ability for the metallic cation to change its coordination environment to a lower one is vital to the oxide ion conductivity of the material. [22]

2.2. Diffraction.

As will be shown in the Experimental, to analyse the compounds synthesised, X-Ray Diffraction (XRD) techniques were applied and their patterns subsequently refined using LeBail and Rietveld refinement. Here the underlying theory behind XRD and the refinement will be briefly explained.

Crystal structures consist of repeating unit cells, which can each be described by the three lengths of their sides (*a*, *b*, *c*) and the angels between these lengths (*α*, *β*, *γ*). Depending on the ratio of these numbers, fourteen Bravais lattices can be assembled, which in turn, based on their symmetry, can be assorted into a total of 230 space groups. Within these unit cells, Miller planes can be found, which are defined by their Miller indices intersecting the *x*, *y*, and *z* axes. These individual planes can be parallel to each other, forming sets.

The Miller planes are important, as waves of light or energy can scatter off points within them. As can be seen on the left of figure 7, taking two parallel X-ray beams, one may hit one layer and the other a parallel layer separated by distance *d*. The second beam will travel slightly further than the first beam, depicted as red before scattering and green after scattering. The extra distance is equal to *d*sin(θ)*, with *θ* being half of the small angle between the incoming and scattered beam, thus leading to the total extra distance travelled by the second beam being *2d*sin(θ)*. Bragg's Law takes this a step further, stating that for constructive interference (as seen on the left in figure 7), the extra distance needs to be equal to an integer times the wavelength of the incoming wave. This can be formulated as:

$$n\lambda = 2dsin(\theta) \tag{2}$$

In this equation's left side, *n* is the integer and *λ* is the wavelength. If instead of *n*, *(n+½)* is chosen, the waves will create destructive interference, as seen on the right in figure 7.

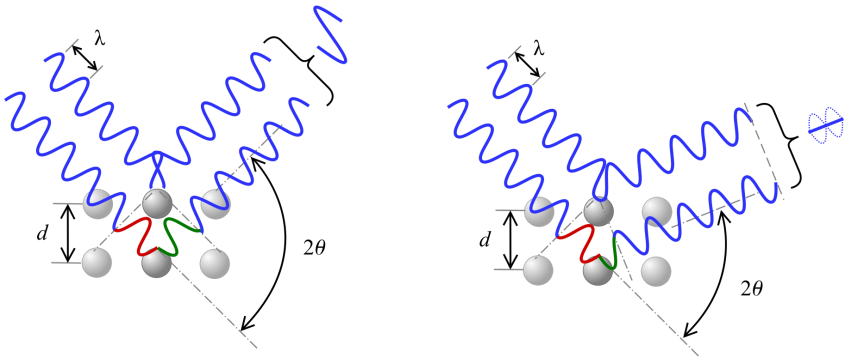

Figure 7. Two waves of energy hitting two parallel planes, showing how Bragg's Law works and how either constructive (left) or destructure (right) interference occurs. [32]

This equation can thus be used to calculate the interatomic distance between two Miller planes, if the wavelength and scattering angle of the beam are known. In XRD monochromatic x-rays are used for this, since the wavelength of x-rays is of the same order of magnitude as the interlayer distance, and the monochromaticity prevents any dispersion. These beams are sent towards the powdered sample, which scatters them without any preferred orientation, after which any waves that are not destroyed through interference are detected by the detector, which measures their intensity. As a result of this, an XRD pattern is created, giving rise to intensity peaks at certain constructive *2θ* angles, depending on the sample. These peaks thus correlate to specific Miller planes in the compound analysed, by which the crystal structure of the sample can be determined.

After the XRD pattern is taken, the structural model can be refined from it by matching the pattern. XRD refinement is an analytical technique used in materials science to determine the crystal structure of a compound. It is performed by applying a theoretical model and matching that model with the measured XRD pattern, from which, depending on the refinement method employed, crystalline data can be gathered. Here we will give a brief explanation on the refinement methods utilised, namely the Le Bail method and the Rietveld method.

The Le Bail method [33] is employed first to determine the lattice parameters. In this method the sample parameters, determined by the unit cell, the zero error, and the parameters determining the peaks shape and width, are changed to give a better profile fitting. To make sure that the programme is not running wild, a first guess needs to be made regarding the compound's space group. This initial guess is made by giving it a file containing the parameters of a similar known compound. When the programme is run well, it should give a good approximation of the compound's lattice parameters, based on the least squares analysis method. Central to the Le Bail refinement is the following formula:

$$I_{obs}(1) = \sum (y_i(obs) * y_i(1)) / y_i(calc) \quad (3)$$

The formula is there to distinguish overlapping peaks from the refinement. Here the $I_{obs}(1)$ is the observed intensity, initially set as an arbitrary value, based on the input given. It is a relative measure between the influence of a Bragg peak ($y_i(1)$) has on the observed diffraction pattern ($y_i(obs)$), by dividing it by the total of all Bragg peaks that may contribute to the observed peak ($y_i(calc) = y_i(1) + y_i(2) + \ldots$). After each iteration, the calculated intensity replaces the initially observed intensity, by which the unit cell parameters are fitted using the least-squares method. This is graphically displayed by seeing the calculated peak move closer to the observed peak. This process is repeated until the calculated peak positions sufficiently overlap and the peak shapes correspond with the observed ones. One thing to watch out for is the absence of the structure factor in this method, leading to some peak intensities being off. This itself is of no consequence to the aim of the Le Bail fit, to obtain the lattice parameters, which is done by accurately fitting the peak position and shape. The intensities will be corrected by the Rietveld refinement, which will take into account the atomic positions and occupancy of them.

Once the Le Bail refinement is complete and the unit cell known, Rietveld analysis [34] can be applied to examine the contents of the unit cell. Much like Le Bail, a theoretical model is compared to the XRD pattern. The theoretical model mainly consists of three sets of

parameters. The first group is the instrumental parameters, determining the instrumental peak broadening, its asymmetry, and the zero point error. Secondly are the unit cell parameters determining the peak position. Thirdly, the intrinsic sample parameters, such as the atomic positions, are taken into account. From refining these three groups, the refinement algorithm automatically computes a Hessian matrix, which is transformed into a covariance matrix, by which it displays a prompt on the graphical user interface when there is a strong correlation between the refined parameters. In the case of this thesis, Rietveld refinement was used to determine the atomic positions, their isotropic atomic displacement parameters, also known as U_{iso}, and their occupancy.

3. Experimental.

In this chapter the method employed, their details, and the reasoning behind that shall be discussed. Generally, the methods can be categorised into three sections; the solid-state synthesis, the X-ray diffraction, and the refinement. These will be discussed in order.

3.1. Solid-state Synthesis.

The solid-state synthesis can be divided into three parts. The first part considers the first calcination step done for the $Ba_3MoNbO_{8.5}$. In the original work of Fop et al. regarding this compound, after grounding and pelletising, the first calcination step was done at 900 °C for 10 hours, whilst the rest of their steps were taken at 1100 °C for 48 hours. Why this was done was not explained, but it was theorised that it was done to let the excess CO_2 escape from the sample. Since this was unproven, it was decided to create two batches of $Ba_3MoNbO_{8.5}$, and let one calcine at 900 °C for 10 hours as described in literature, and one sample at 1050 °C for 48 hours.

All samples were synthesised using the same general procedure. Stoichiometric equivalents of barium carbonate ($BaCO_3$, 99.86%, Chem-Impex), molybdenum trioxide (MoO_3,), niobium pentoxide (Nb_2O_5, 99.9985%, Puratronic) were weighed. The precursors were mixed and crushed together using a pestle and mortar, to obtain two grams of the sample powder mixture. The powder mixtures were then pelletised into 20 millimetre pellets using a hydraulic press and corresponding die-press set, under a pressure ranging between 2250 and 4500 kg. The pellets were carefully inserted into their own crucible to be calcined in the furnace for and with their respective time and temperature. The samples were given the names F001 for the one calcined at 1050 °C for 48 hours, and F002 for the one calcined at 900 °C for 10 hours. Both samples were heated at +50 °C/h and cooled down at -50 °C/h. The required mass, calculated using the stoichiometry of the product and its precursors, as well as the weighted mass for each sample, are displayed in table 1.

	Calculated required mass (g)	**Actual weighted mass (g)**	
	F001 & F002	**F001**	**F002**
$BaCO_3$	3.213822	3.2124	3.2143
MoO_3	0.781388	0.7812	0.7808
Nb_2O_5	0.721484	0.7219	0.7208

Table 1. Mass of precursors used to synthesise two grams of $Ba_3MoNbO_{8.5}$ for samples F001 and F002.

After this first calcination an XRD measurement was taken (as detailed further on) to evaluate the extent of the reactions and decide whether the first calcination at a lower temperature and shorter time proves useful. As will be discussed further in the following chapter, both samples showed side phases after their first calcination, but F001, performed at a higher temperature and longer time, showed significantly less impurities. Thus in any further sample synthesis, the first calcination step was taken to be at the same time length and temperature as its subsequent steps.

To synthesise phase pure products, further calcination steps were taken. Both samples were reground, pelleted, and calcined at 1100 °C for 48 hours each step. For these steps the

heating and cooling rates were increased to +150 °C/h and -100 °C/h, respectively. The total reaction follows this reaction formula:

$$6\ BaCO_3 + 2\ MoO_3 + Nb_2O_5 \rightarrow 2\ Ba_3MoNbO_{8.5} + 6\ CO_2 \quad (4)$$

This step was repeated until phase purity was reached for both samples.

Once the $Ba_3MoNbO_{8.5}$ samples had reached phase purity, an attempt was made at recreating the $Ba_3MoNb_{1-x}V_xO_{8.5}$ series, with x = 0.1, 0.2, 0.3, and 0.4. These having been made next, they have been aptly named F003, F004, F005, and F006, respectively. For each sample the objective was to produce two grams. The calculated required and the actual weighed mass for each sample have been denoted in table 2.

	Calculated required mass (g)				**Actual weighed mass (g)**			
	F003	**F004**	**F005**	**F006**	**F003**	**F004**	**F005**	**F006**
	$Ba_3MoNb_{0.9}V_{0.1}O_{8.5}$	**$Ba_3MoNb_{0.8}V_{0.2}O_{8.5}$**	**$Ba_3MoNb_{0.7}V_{0.3}O_{8.5}$**	**$Ba_3MoNb_{0.6}V_{0.4}O_{8.5}$**	**$Ba_3MoNb_{0.9}V_{0.1}O_{8.5}$**	**$Ba_3MoNb_{0.8}V_{0.2}O_{8.5}$**	**$Ba_3MoNb_{0.7}V_{0.3}O_{8.5}$**	**$Ba_3MoNb_{0.6}V_{0.4}O_{8.5}$**
$BaCO_3$	3.232278	3.250898	3.269734	3.288790	3.2316	3.2512	3.2693	3.2887
MoO_3	0.785876	0.790403	0.794983	0.799616	0.7848	0.5838	0.7952	0.7993
Nb_2O_5	0.653065	0.583846	0.513825	0.442988	0.6533	0.7898	0.5143	0.4426
V_2O_5	0.049651	0.099874	0.150679	0.202076	0.0499	0.1002	0.1503	0.2022

Table E2. Mass of precursors used to synthesise two grams of $Ba_3MoNb_{1-x}V_xO_{8.5}$ for samples F003 till F006.

Having seen that the procedure from F001 produces a higher quantity of desired product after the first calcination step, it was decided to keep the higher temperature and longer calcination time for the calcination steps for these samples. All precursors used were the same as in the previous experiments, with the addition of vanadium pentoxide (V_2O_5, 99.99%, Aldrich) Each step was performed at 1100 °C for 48 hours, with a heating rate of +150 °C/h and a cooling rate of -100 °C/h. To form the desired product, the reaction should following this reaction formula:

$$6\ BaCO_3 + 2\ MoO_3 + (1\text{-}x)\ Nb_2O_5 + x\ V_2O_5 \rightarrow 2\ Ba_3MoNb_{1-x}V_xO_{8.5} + 6\ CO_2 \quad (5)$$

3.2. X-ray Diffraction.

After every calcination step X-ray diffraction patterns were collected to monitor the progress of the synthesis. The laboratory X-ray powder diffraction patterns were collected using a PANanalytical X'Pert Pro X-ray diffractometer equipped with a Cu Kα source (1.54Å) operated at 45kV, 40mA. The XRD patterns were recorded in the range 10° < 2Θ < 100°. A LaB6 NIST standard (NIST660C) was used for both the calibration and performance qualification of the diffractometer. Measurement times varied from 8 minutes for every calcination step, to monitor the synthesis, to 32 minutes for the XRD patterns used in refinement.

3.3. Refinement.

The XRD patterns were refined using both the LeBail and Rietveld methods subsequently. The refinement of the XRD patterns were performed using the GSAS-II software. The refinement was approached in the following manner: The XRD data was, acquired as an .xrdml file, was converted into a .raw file using the PowDLL software, after which it was imported into the GSAS-II software. [35] Upon importing, the programme asks for a parameter file, in the form of .xryprm file. Upon importing this file, the programme shows the XRD pattern. To remove any unnecessary noise, the 2θ front limit was set to 17°. To remove further background noise, a background line must be fitted. This is performed by selecting points just below the XRD pattern and letting the programme fit a polynomial line to them. To attain a more accurate refinement, it is essential to separate the background from the peak, thereby not taking away any counts belonging to the peak. Once the background has been fitted, no further refinement must be done on it to keep any further refinements consistent.

To start the refinement of the crystal structure, a first approximation regarding its structure needs to be made. This is performed by importing one or more Crystallographic Information Files (.cif), containing the crystallographic data on a single structure, belonging to the targeted end product and, if showing any unidentifiable peaks, any possible and likely side phases. In these refinements, only the XRD patterns of the end product were refined, and thus only the .cif file from the $Ba_3MoNbO_{8.5}$ structure was imported. The file was obtained from the work of Fop et al. in 2016 [18]. Details on the .cif file can be obtained from the Supporting Information of his work.

Firstly, the LeBail refinement was performed to extract the lattice parameters. By refining them along with the instrumental parameters, such as the zero shift and the asymmetry, the simulated diffraction pattern was fitted to follow the lineshape of the actual diffraction pattern. To make the peaks generally wider, and thus more Lorentzian, the X, Y, Z parameters were refined, whilst to make the peaks more narrow the Gaussian parameters of U, V, and W, were refined. The crystallite size and the microstrain could also be refined and kept if their refinement improved the lineshape. The Le-Bail fit can be deemed concluded once a satisfactory fit has been realised. It is worth noting that a good match between the observed data and simulated pattern can be determined from the features of the difference plot (as will be shown in figure 14 of chapter 4).

Secondly, the Rietveld refinement was performed to refine the location, fraction, and U_{iso}, of the atoms within the unit cell. Their locations were refined first, followed by their U_{iso}, and then their fraction, for them to direct to their actual numbers. This was followed by a refinement in which all three factors were refined together, thereby conceivably showing little further change. Once done, the covariance matrix was printed to see if any hard correlation

exists between the refined parameters and automatically acquired their estimated standard deviations by taking the square root of the variances in the covariance matrix.

The covariance matrix, as far as this thesis is concerned, is not used to determine the goodness of fit. A good fit was determined by inspecting the difference profile plot, and this is probably the best way of following and guiding a refinement process: either Le-Bail or Rietveld. The refinement algorithm will interpret the difference profile to the following quantities: least-squares, the weighted profile R factors, and goodness of fit or the chi-square. The covariance matrix is however a manifestation of the computational engine (analytic hessian) used for the refinement, and it was thus implemented in printing the error on the refined parameters after a good fit has been actualised. The x- and y-axes of a covariance matrix contain the refined parameters in the same order, while the colour shows the magnitude of the correlation between the refined parameters. The green diagonal depicts the variances, while the rest of the plot contains the covariances. The variances illustrate the errors on each refined parameter, and the covariances show the correlation between each of the refined parameters.

4. Results & Discussion.

In this section each of the results gathered from the experiments and analyses will be shown and explained. First the synthesis of the $Ba_3MoNbO_{8.5}$ samples will be discussed, taking a closer inspection at the first calcination step, followed by the rest of the calcination. Subsequently, the samples containing vanadium substitution in the form of $Ba_3MoNb_{1-x}V_xO_{8.5}$ with x = 0.1, 0.2, 0.3, and 0.4, will be discussed, including their synthesis, which follows the same procedure as the $Ba_3MoNbO_{8.5}$ samples, and the refinement of their structural models. In particular, the LeBail refinement brings an interesting trend in lattice parameters that could be linked to Vegard's Law and the Rietveld refinement gives great insight into the location of the atoms, in particular the vanadium, and the occupation of the M1 site, offering deeper insight into this material, beyond the state-of-the-art of the field.

4.1. $Ba_3MoNbO_{8.5}$.

4.1.1. First Calcination Step.

As stated in the experimental section, two 2-gram samples were made by carefully weighing the precursors, grounding them together, and pelleting them. The samples were given the names F001 and F002. In the original paper from Fop et al. [18], the first calcination was done at 900 °C for 10 hours, however, it was not explained why this was done. Therefore it was decided to try two different calcination reactions by varying the temperature and the

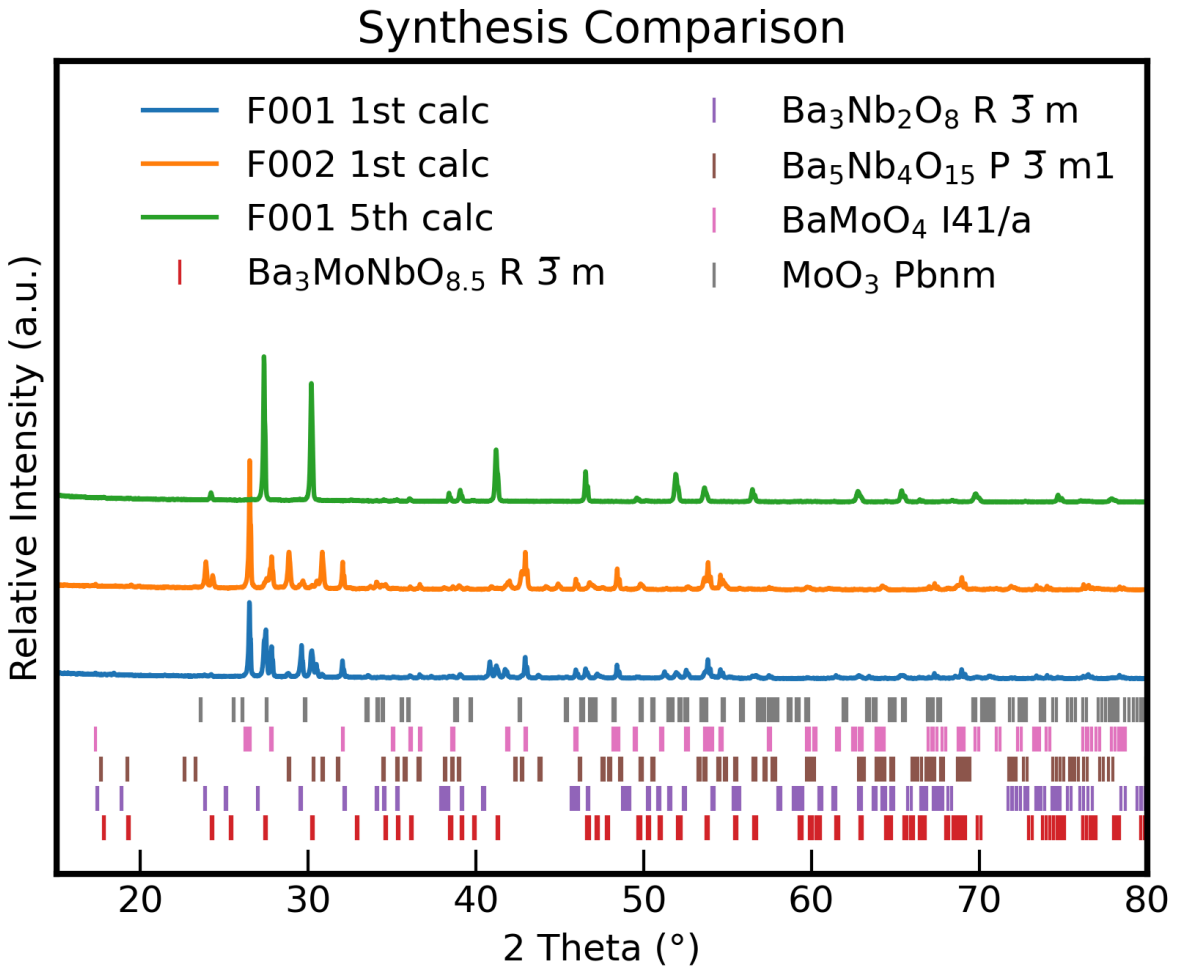

Figure 8. XRD patterns comparing the first calcination of F001 and F002. To normalise it to the largest peak of the end product and highlight it, the XRD pattern of the fifth calcination of F001 is also given.

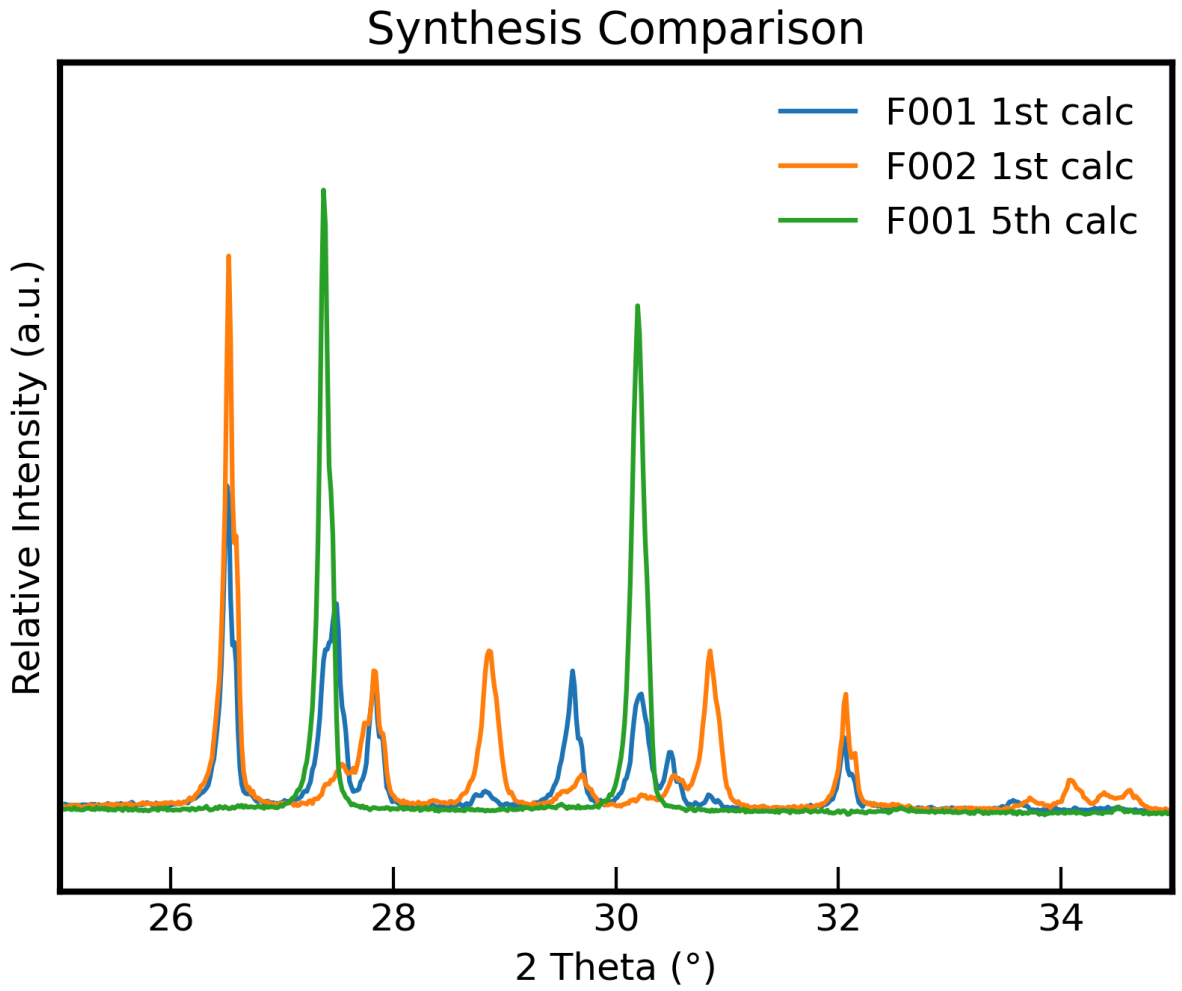

Figure 9. Region from 25° to 35° 2θ of the XRD patterns of the first calcination of F001 and F002. To normalise it to the largest peak of the end product and highlight it, the XRD pattern of the fifth calcination of F001 is also given, in order to give a better comparison.

time. For F001 a calcination at 1050 °C for 48 hours was chosen, similar to subsequent steps in the literature, whilst for F002 has its first calcination as stated in literature. The XRD patterns of the first calcination of F001 and F002 are displayed as stacked in figure 8, allocating the phases present in the structures. In figure 9, the 2θ range was chosen to highlight the highest intensity reflections of the side phases, either precursors or intermediate products, and the main phase, and the patterns were made to overlap to better see the difference in peak height between the F001 and F002 patterns. In green the most intense reflection for the targeted phase is at 27.4° (105), with its second largest reflection found at 30.2° (110). These peaks are mainly prevalent for F001. The other peaks belong to different phases and were identified using the Match! Software [36]. By constraining the search to the atoms and ions contained within the precursors, as in Ba^{2+}, Mo^{6+}, Nb^{5+}, O^{2-}, and C, the side phases were identified. As can be seen from figure 8, one of the side phases identified is that of $Ba_3Nb_2O_8$, which has its sharpest reflection around 29.5° (105), showing a large peak for F001, but a rather flat one for F002. Another barium and niobium containing compound has been identified as $Ba_5Nb_4O_{15}$, with its largest reflections at 28.8° (103) and 30.8° (110) On the left side of figure 9 a highly present peak is found at 26.5°, which has been identified as belonging to the 112 plane of $BaMoO_4$, having another two peaks at

around 27.8° (004) and 32.1° (200). The first peak especially shows a large difference between F001 and F002, with the larger peak belonging to the latter. Finally, some minor peaks on the F002 XRD pattern can be identified to belong to one of the precursors, MoO_3, with its most notable reflections found at 27.5° (021) and 34.1° (111).

It was expected that a longer calcination time and higher calcination temperature would result in an increase of the desired end product and a decrease in the amount of side phases, since the addition of more energy to the system and more time to diffuse would allow for better transport along the crystal structure. As can be seen from figure 9, comparing between the peaks for the first calcination of F001 and F002, the peaks belonging to the side phases are much more pronounced for F002, especially looking at $Ba_5Nb_4O_{15}$ and $BaMoO_4$. In the F001 sample there is still an amount of $BaMoO_4$, but in a much lower quantity than F002. It does however show the $Ba_3Nb_2O_8$ side phase, which is barely found in F002. The peaks belonging to $Ba_5Nb_4O_{15}$ in F002 and $Ba_3Nb_2O_8$ in F001 do have similar intensities, which may mean that at higher temperatures of F001 compared to F002, the former reacts away to the latter. F002 also shows a very shallow peak for the targeted phase, implying that the reactions with the pellet first go to $BaMoO_4$ and $Ba_5Nb_4O_{15}$, before reacting onward to $Ba_3MoNbO_{8.5}$, likely through another side phase in the form of $Ba_3Nb_2O_8$. Furthermore, in F002 there is still evidence left of small amounts of the MoO_3 precursor. It can therefore be suggested that the higher temperature (1050 °C as opposed to 900 °C) and the longer calcination time (48 hours as opposed to 10 hours) are beneficial to the overall reaction. From this we can deduce that there is a solid state reaction happening among the reactants in the pellet.

As to why there are still multiple phases left even in the F001 sample, there could be a multitude of reasons explaining the situation. The most obvious reason could be the insufficient amount of diffusion occurring, even at elevated temperatures and a longer span of time. The ions within the precursors also likely play a role in the diffusion behaviour; Ba^{2+} has a much smaller charge than either Mo^{6+} or Nb^{5+}, and thus requires much less energy to travel through the ionic point defects of the matrices. The ionic diffusion of the higher charged ions is thus mitigated by the energy required to move around these point defects, as the high energy makes it less likely to occur.

Another reason may be the spatial arrangement of the precursors once the pellet was pressed. For solid state reactions to occur there needs to be close contact between the surfaces of the precursor phases The powders were grounded together in an attempt to create an uniform mixture. However, this process is of course not perfect, as the powders were grounded in a pestle and mortar, and thus human errors such as placing too little force can or a less uniform distribution can occur, giving the possibility that some portions of the pellet contained a higher concentration of certain precursors. For example, it could be that one part of the pellet mainly contained $BaCO_3$ and Nb_2O_5, whilst another part mainly consisted of $BaCO_3$ and MoO_3, leading to an inhomogeneous dispersion of the two transition metallic cations and the formation of localised $Ba_3Nb_2O_8$ and $BaMoO_4$, respectively.

Nevertheless, the desired phase was forming after the first calcination of both samples, although in a higher amount for F001. Clearly, one calcination step was insufficient to obtain a phase pure sample, thus leading to further calcination steps in order to increase the purity of the sample. It was also concluded that the process for F001 worked better, and thus a similar approach of a higher temperature and a longer calcination time were continued, as was also done in literature after the first calcination.

4.1.2. Subsequent Calcination Steps.

Since the calcination conditions resulted in a smaller concentration of side phases for sample F001, it was chosen over sample F002 to continue undergoing further calcination steps. The XRD patterns obtained after every calcination step are shown in figure 10. The lowest XRD pattern in blue is that of the first calcination step, and as they are followed up, the fifth and final calcination step is depicted in violet. Below them the peaks belonging to the target phase and formed side phases are denoted. According to Fop et al. [18], the targeted end phase of $Ba_3MoNbO_{8.5}$ has a hexagonal perovskite structure of the space group $R\bar{3}m\ H$. The structure of $Ba_3MoNbO_{8.5}$ in this space group exhibits a XRD pattern with its most pronounced reflections found at 27.4° {015} and 30.2° {110}.

As can be seen again in figure 10, the most pronounced peak after the first calcination of F001 is at 26.5°, which is inconsistent with the pattern expected for $Ba_3MoNbO_{8.5}$. However, it can be indexed for the 112 plane of $BaMoO_4$. Looking at the diffraction pattern of the first calcination as a whole, there are multiple other peaks that have been identified as intermediate products of the solid state reaction, such as $BaMoO_4$ and $Ba_3Nb_2O_8$, as shown in the previous section. One may also contemplate whether any precursors, such as $BaCO_3$, MoO_3, and Nb_2O_5, were left over, but no peaks could be identified as such. As more and more calcination steps occur, the amount and size of the peaks belonging to side phases disappear and the peaks belonging to $Ba_3MoNbO_{8.5}$ increase in size.

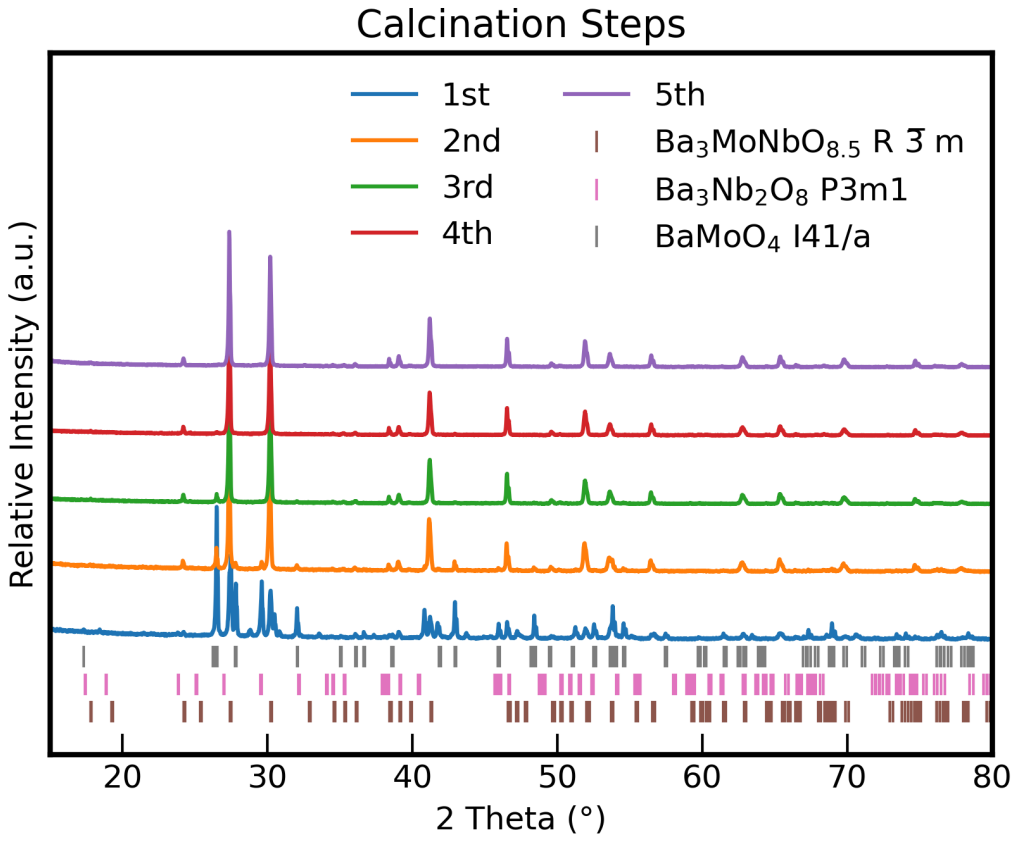

Figure 10. XRD patterns of intermediate calcination steps for F001 sample. Matched phases displayed as vertical bars.

In figure 11 this has been highlighted by taking the range in which the most prominent peaks occur and overlapping the XRD patterns to show the increase and decrease of the peaks over the calcination steps. The six most prominent reflections are located at 26.5°, 27.4°, 27.8°, 29.6°, 30.2° and 32.1° 2θ. As more calcination steps occur and thus the solid state reaction progresses, it can be seen that the peaks at the 26.5°, 27.8°, 29.6°, and 32.1° 2θ reflections shrink, whilst the peaks at 27.4° and 30.2° 2θ increase in size. The decreasing peaks at 26.5° and 27.8° have earlier been identified to belong to the {112} and {004} planes of $BaMoO_4$, respectively, whilst the ones at 29.6° and 32.1° belong to the {105} and {110} planes of $Ba_3Nb_2O_8$, respectively. Thus a decrease in their size over the amount of calcination steps signifies them reacting away. On the other hand, one can see the two increasing peaks belonging to the {015} and {110} planes of $Ba_3MoNbO_{8.5}$, thereby evidencing its formation. After five calcination steps there is no more increase in the peaks of the desired product, nor decrease in the peaks belonging to side phases.
These XRD patterns would therefore imply that the system as a whole moves towards a more thermodynamically stable phase over the calcination steps. This thermodynamically stable composition is the desired product, $Ba_3MoNbO_{8.5}$. It could however be speculated that the mechanism of the reaction towards $Ba_3MoNbO_{8.5}$ requires the intermediate step in the formation of $BaMoO_4$ to form the hexagonal perovskite. This reaction is similar to the formation of $BaTiO_3$, which is synthesised from $BaCO_3$ and TiO_2, but has an intermediate phase of Ba_2TiO_4 [37].

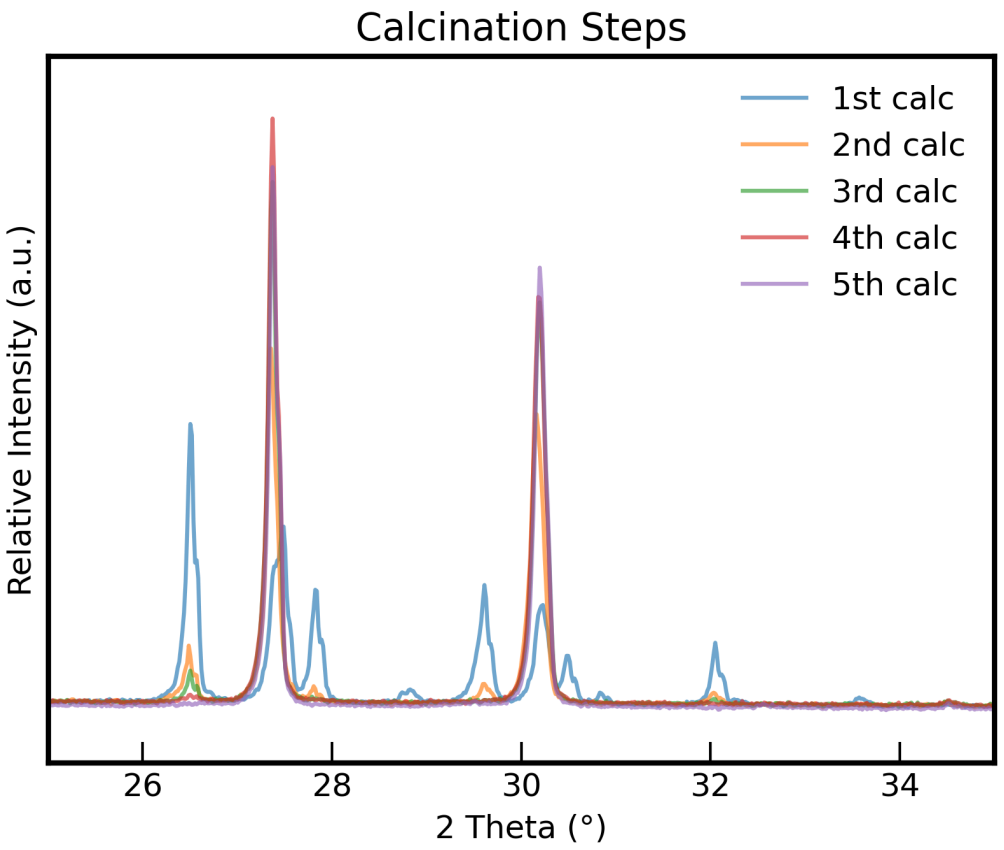

Figure 11. Region from 25° to 35° 2θ of the XRD patterns with overlapping intermediate calcination steps for the F001 sample.

4.2. Vanadium Substitution.

With the success of the synthesis of $Ba_3MoNbO_{8.5}$, and its synthesis conditions and method verified to be working adequately, an attempt was made at synthesising a composition in which V^{5+} partially substitutes Nb^{5+}. This was to be achieved by stoichiometrically substituting Nb_2O_5 with V_2O_5, depending on the amount of vanadium doping required. As literature would suggest, this would lead to the formation of $Ba_3MoNb_{1-x}V_xO_{8.5}$, with x = 0.1, 0.2, 0.3, and 0.4.

4.2.1. Synthesis of $Ba_3MoNb_{1-x}V_xO_{8.5}$.

The $Ba_3MoNb_{1-x}V_xO_{8.5}$ samples were given the names F003 through F006, with x = 0.1 for F003 and x = 0.4 for F006. The synthesis of these samples was analogous to the synthesis of the $Ba_3MoNbO_{8.5}$ F001 sample; the same method of mixing and grounding the precursor powders was performed, with them being pelleted and calcined in the furnace. For each calcination step the temperature was set to 1100 °C and the calcination time was kept at 48 hours, since the higher temperature and longer time were deemed beneficial to the reaction.
During the synthesis similar side phases were encountered as during the synthesis of F001, such as $BaMoO_4$ and $Ba_3Nb_2O_8$. It is also likely a form of $Ba_3V_2O_8$ was present in small amounts, but its peak in the XRD pattern would overlap with that of $Ba_3Nb_2O_8$. However, according to the XRD data (See Appendix A1-A5), after the first calcination of the vanadium-based samples there is a larger amount of the desired end product, evidenced by the larger peak around the 27.4° {015} 2θ reflection, in comparison to F001. Interestingly enough, whilst the initial peak at the 26.5° {112} reflection of $BaMoO_4$ for the vanadium-based samples is around the same intensity as that for F001, it decreases in height at a much slower rate; for F001 it looks more like a curbed hill after the second calcination, whilst for all the vanadium-based samples it is still a defined peak.
The clear distinction between F001 and vanadium-based samples is the addition of V^{5+} in the form of V_2O_5, by substituting the Nb^{5+} ions. One could think of several hypotheses as to why this difference leads to a higher initial purity of the end product and a larger retention of $BaMoO_4$. The first that comes to mind is the higher mobility of V^{5+} as opposed to Nb^{5+}, since they experience the same charge effects, but the V^{5+} ion has a smaller ionic radius than Nb^{5+} (68 pm vs. 78 pm). This higher mobility allows it to diffuse further and thereby increase the amount of end product being formed. Another reasoning could be the melting point of the precursors used; V_2O_5 has a relatively low melting temperature of only 680 °C, as opposed to Nb_2O_5 with a melting temperature of 1500 °C. Noting that the melting temperature of Nb_2O_5 is much higher than the calcination temperature, one must keep in mind that the temperature at which a solid material becomes mobile enough to diffuse, occurs at half the melting temperature, as stated by Tammann's rule. Similarly, this could mean that the vanadium is more mobile and possibly easier to react with, again allowing for a larger amount of end product to be formed in the time given. It could also be taken a step further in that the initial reaction of V_2O_5 with the $BaCO_3$, MoO_3, and Nb_2O_5 gives localised clusters of $Ba_3MoNb_{1-x}V_xO_{8.5}$ with a relatively high amount of V^{5+}, thereby inhibiting the reactions between $BaMoO_4$ and $Ba_3Nb_2O_8$. This would explain why there is a larger amount of end product after the first calcination, but further calcination sees a larger amount of the retained $BaMoO_4$ side phase. Although the $Ba_3Nb_2O_8$ peak is also slightly larger in the vanadium-based samples, this difference is smaller and thereby harder to qualify.

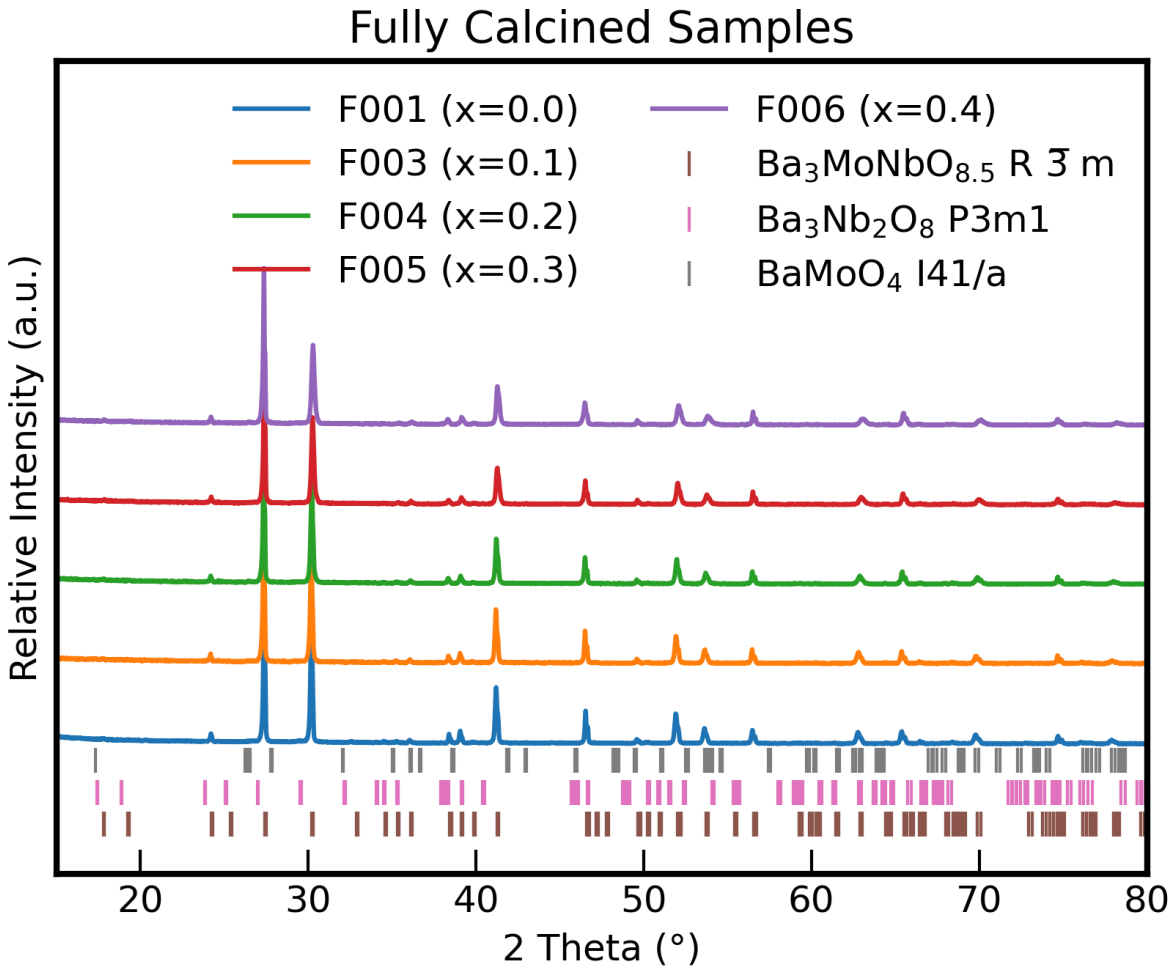

Figure 12. XRD patterns of fifth calcination step for five samples (F001, F003, F004, F005 and F006)

Similar to $Ba_3MoNbO_{8.5}$ of the F001 sample, no further significant changes were detected in the XRD pattern after the fifth calcination. Figure 12 gives an overview of the XRD patterns of all five samples after their fifth calcination. The peaks shown belong to the desired end product of $Ba_3MoNb_{1-x}V_xO_{8.5}$, with no further peaks belonging to side phases present, evidencing phase purity.

4.2.2. Refinement of the $Ba_3MoNb_{1-x}V_xO_{8.5}$ samples.

After the phase pure vanadium-based samples were synthesised, a final XRD measurement was taken of each sample (as displayed in figure 12). The XRD patterns were then refined to detail the crystal structure of the obtained products. The first method employed was the LeBail method, in order to obtain the lattice parameters. By replacing the Nb^{5+} ion with the smaller V^{5+} ion, it is to be expected that the lattice parameter shrinks. This expectation could also be linked to Vegard's law. This law states that the lattice parameter of a solid solution mixture of two compounds having the crystal structure will correspond linearly to the ratio of the mixture. This is denoted in the following formula:

$$a_{A(1-x)B(x)} = (1-x)a_A + x^*a_B \quad (6)$$

Here *a* is the lattice parameter, the *A* and *B* subscript denoting the compound, and *x* being the fraction of compound *B* present in the mixture. This could be associated with the vanadium substitution, where compound *A* would be $Ba_3MoNbO_{8.5}$ and compound *B* would be $Ba_3MoVO_{8.5}$. Although $Ba_3MoVO_{8.5}$ is not a stable compound, according to Tawse et al. [26], it would have a theoretical set of lattice parameters. Thus one hypothesis is that the lattice parameter of $Ba_3MoNb_{1-x}V_xO_{8.5}$ follows a downward linear fit.

From the LeBail fit the lattice parameters were extracted for each vanadium-based sample, as well as for the mother material. These are denoted in figure 13, with the *a* and *c* parameters, as well as the volume. The *b* parameter in hexagonal perovskite structures is the same as the *a* parameter. From the first part of the figure, we can see a clear decrease in the lattice parameter *a*. This result matches the expectation of the impact vanadium has, although it does not quite match the linear fit Vegard's law would suggest. However, in the second part of the figure the *c* parameter clearly increases. This does not match with what was expected, based on the ionic radii of the cations involved in the chemical substitution, but was also seen in previously conducted research. Despite the increase of the *c* parameter, the volume does decrease. This is due to its higher dependence on the *a* parameter, which is used for both *a* and *b* parameters.
The trend observed for the *a* parameter could indeed be explained by our hypothesis, in that the smaller radius of V^{5+} compared to Nb^{5+} is what causes its decrease. This trend is also resumed in the volume of the unit cell, which also decreases due to the smaller radii of V^{5+}, irrespective of the increase of the *c* parameter. Thereby, the trend on the *c* parameter is somewhat more difficult to explain. One possibility is the effect of the second-order Jahn Teller distortions on the structure. V^{5+} is a stronger distorter than Nb^{5+}, due to its smaller radius whilst maintaining the same charge. This effect distorts polyhedral complexes by either elongating them or compressing them to remove symmetry from a system to compensate for an unequal distribution of electrons. This leads to an out-of-centre displacement, which may cause a higher level of repulsion between the cations along the distortion axis, thereby elongating the unit cell in the *c* direction. In order to confirm this, the *z* coordinate must be evaluated, which will result from the Rietveld refinement later on. Another interpretation is that the V^{5+} ions force the M1 site to be more tetrahedrally coordinated. Whilst the octahedral coordination provides a coplanar palmierite layer of $BaO_{2.5}$, the tetrahedral coordination causes the single oxygen coordinated to be out-of-plane, as seen in figure 6a, either above or below depending on whether the tetrahedron is below or above the plane, respectively. This causes the O^{2-} anions to move in a sinusoidal wave along the palmierite layer, when seen from the *ac*-plane. Thus to accommodate the more tetrahedral coordination of V^{5+}, the crystal structure could elongate itself along the *c* direction.

Whilst this gives good insight on the crystal structure, it says nothing about the location or occupation of the atoms within. Therefore, the next part will entail the results gained from the Rietveld refinement and discuss them.

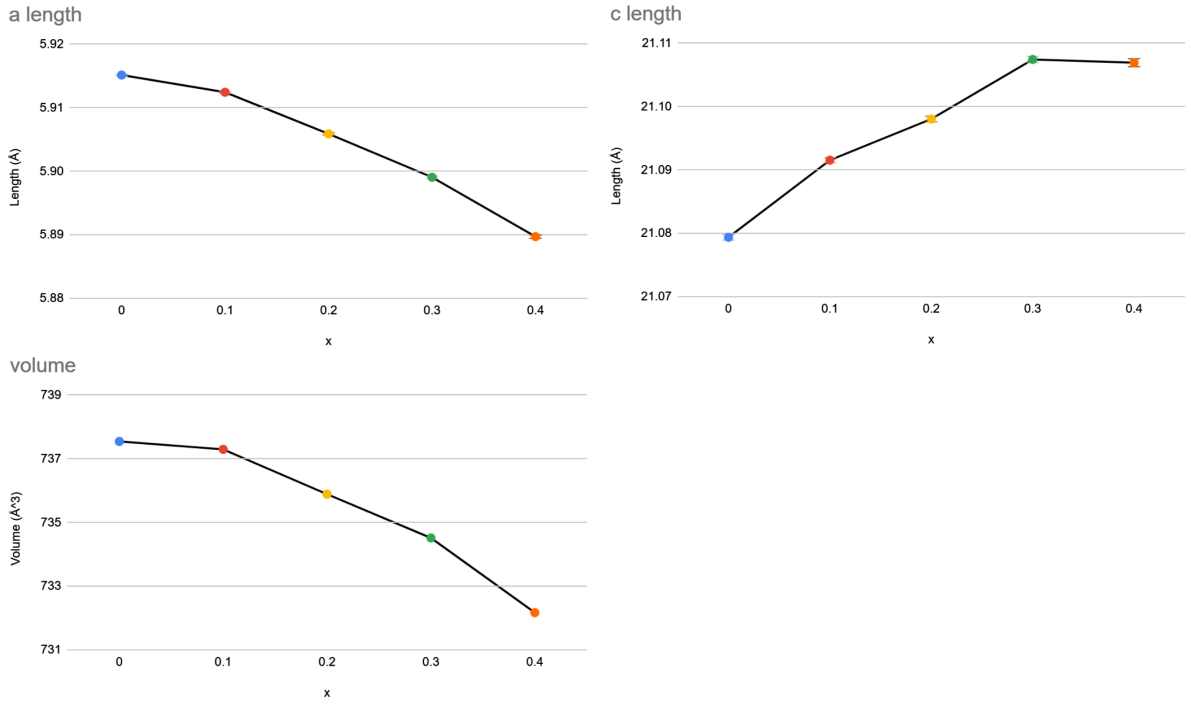

Figure 13. Graphic representation of the change in the lattice parameters a and c, and the volume, over the vanadium content within $Ba_3MoNb_{1-x}V_xO_{8.5}$.

From the Rietveld refinement it was expected to find V^{5+} have a relatively high occupation on the M1 site, as it is the only one of the two sites that is able to have tetrahedral coordination, which V^{5+} prefers over octahedral coordination. In the work of Fop et al. all three cations (Mo^{6+}, Nb^{5+}, and V^{5+}) were spread among the M1 and M2 sites, with vanadium split 60% on the M1 site and 40% on the M2 site for $Ba_3MoNb_{0.9}V_{0.1}O_{8.5}$. They saw that this split became more uneven with larger substitution, leading to 82.5% of the vanadium occupying the M1 site for $Ba_3MoNb_{0.6}V_{0.4}$, even then the percentage of both the total amounts of Nb^{5+} and Mo^{6+} increased on the M1 site. This homogeneous distribution of V^{5+} throughout the structures is disputed by our analysis of the XRD patterns of $Ba_3MoNb_{1-x}V_xO_{8.5}$ with x = 0.1, 0.2, 0.3, and 0.4.

To confirm whether our hypothesis is correct, the Rietveld refinement was performed. For an overview of the tabulated results, the images of the Rietveld fits, and the covariance matrices, please refer to Appendix A6-A20. Here, Mo^{6+} and Nb^{5+} were chosen to both be Nb^{5+}, as XRD is unable to accurately distinguish between the two. This is due to the atoms having identical electron clouds, thus being isoelectronic with the electron configuration of krypton. Using neutron diffraction, one could distinguish between, but alas, this was not available to us at the time of experiments.

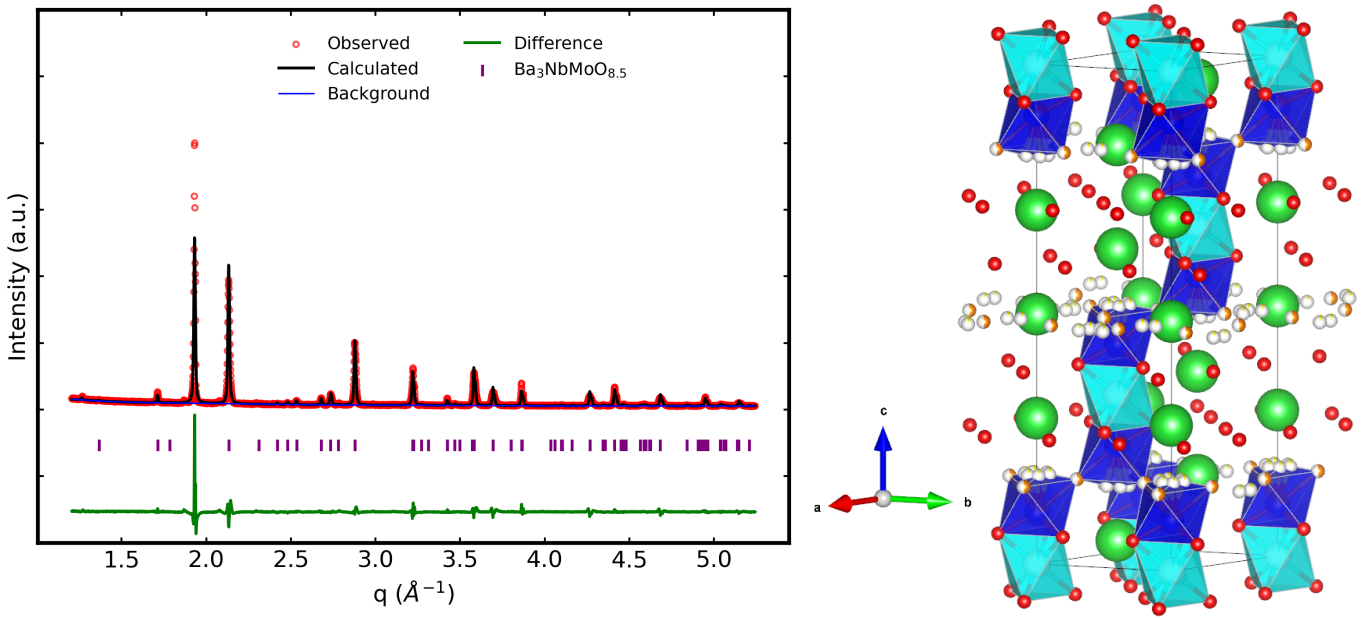

Figure 14. Rietveld fit to the structural model of $Ba_3MoNb_{0.6}V_{0.4}O_{8.5}$ (F006) from X-ray diffraction data (left) and visual representation of the structure and occupation of $Ba_3MoNb_{0.6}V_{0.4}O_{8.5}$, with Ba^{2+} in green, the M1 site in dark blue, the M2 site in cyan, the O1 site in red, the O2 site in orange, and the O3 site in yellow (right).

After having gained the lattice parameters from the LeBail refinement, some restraints were introduced in the Rietveld refinement. To remind one of the structure and refer to colours between parentheses mentioned in the upcoming section, please refer to figure 14. First of all, the z-coordinates of the M1 site were constrained to be the same for both Nb1 (Nb^{5+} & Mo^{6+}) and V1 (dark blue), but left free to vary as a singular unit. This was not necessary for the M2 site, as its location is always situated at (0,0,0). The U_{iso} of both Ba^{2+} atoms (green) were also constrained in the same manner, as well as the U_{iso} for all metallic cation sites. To maintain the stoichiometry of the samples, both the total fraction of V^{5+} and of the combined fraction of Nb^{5+} and Mo^{6+} were constrained. This was done in the following manner, taking into account the multiplicity of the sites:

$$f_{Nb1} * 6 + f_{Nb2} * 3 = 6 - 3x \quad (7)$$

$$f_{V1} * 6 + f_{V2} * 3 = 3x \quad (8)$$

With f denoting the fraction of the subscripted compound and x being the total fraction within the $Ba_3MoNb_{1-x}V_xO_{8.5}$ stoichiometry. During the refinement, V^{5+} was thus left free to occupy both the M1 and M2 site, either splitting up in fractions or entirely localising on one site, in search for the best match with the relative intensities of the experimental XRD pattern.
This Rietveld refinement has produced the following data; location of atoms, their occupancy, and their U_{ISO}. These are graphically represented in the upcoming figures. The first figure, figure 15, shows the fractional occupations of Mo^{6+} and Nb^{5+}, and V^{5+}, on the M1 and M2 site. First taking a look at the compound without any vanadium substitution (F001, *x* = 0), it can be seen that neither the M1 site, with a fraction of 0.92, nor the M2 site, with a fraction of 0.16, is fully occupied. This shows a clear preference for the M1 site by molybdenum and niobium.

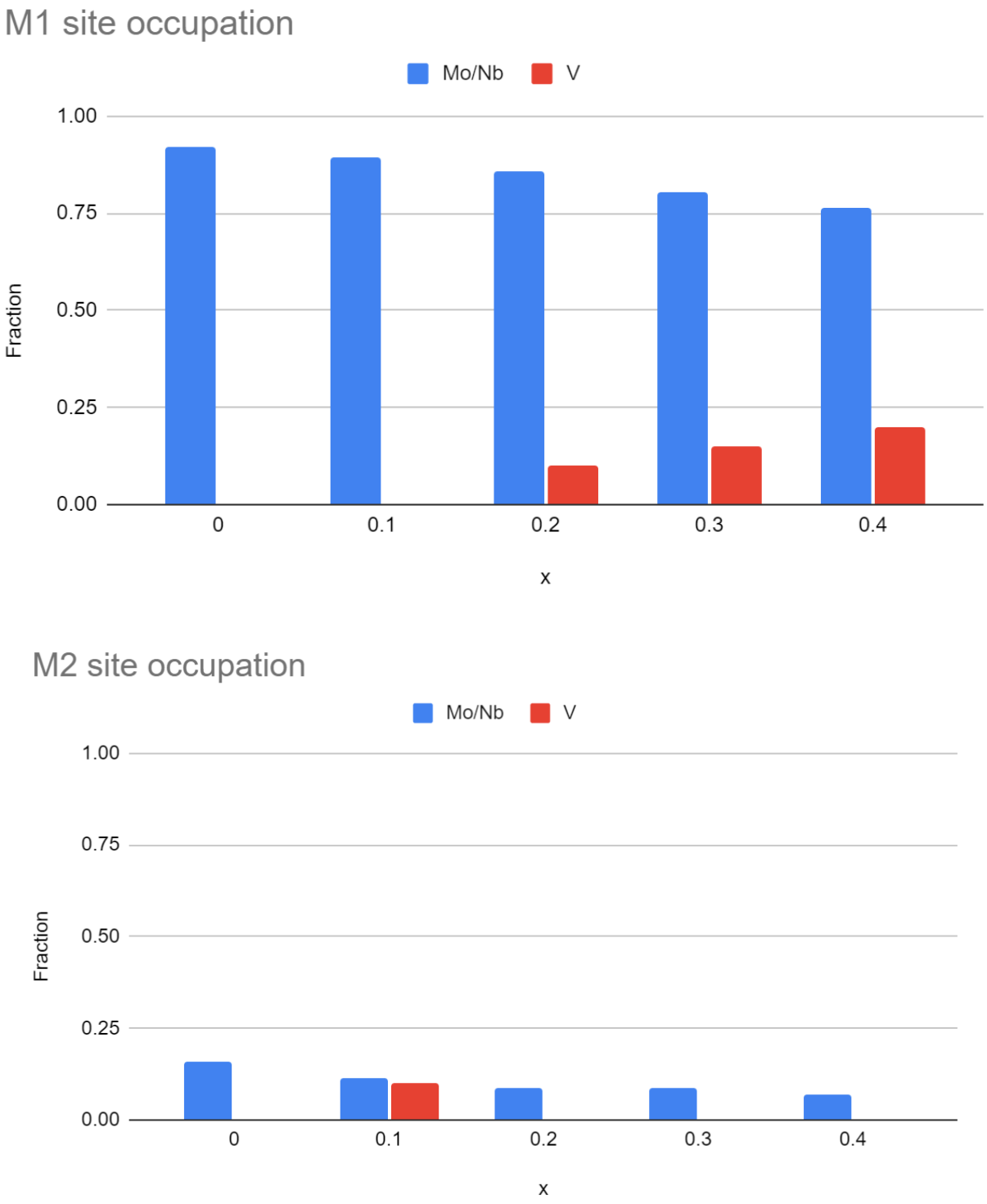

Figure 15. Fractional occupation of the M1 and M2 sites by Mo/Nb and V, acquired from the Rietveld refinement of the XRD patterns for the $Ba_3MoNb_{1-x}V_xO_{8.5}$ samples, with x = 0.0, 0.1, 0.2, 0.3, and 0.4.

These fractional occupancies are similar to those acquired from neutron powder diffraction (NPD) data in earlier reports by Fop et al., with their report from 2016 [18] detailing M1 and M2 occupancies of 0.926 and 0.148, and their work from 2020 [22] having 0.886 and 0.114,

respectively. Seeing how these results are comparable, it can be said that the Rietveld refinement for this sample was performed well, and that the methodology behind it works.
Continuing with the vanadium substituted samples, as stated before, it was expected that V^{5+} would preferentially occupy the M1 site. From the Rietveld refinement, in which V^{5+} was free to occupy any or either of the two cationic sites (M1 and/or M2), V^{5+} clearly chose one site over the other, after which it was locked to that site. In the case of $x = 0.1$, it was preferential to the M2 site, whilst for every other sample containing vanadium, it seemingly preferred to be entirely located on the M1 site. Mo^{6+} and Nb^{6+} showed an overall decrease of their total fraction upon doping with vanadium, thereby decreasing their fractional occupation on both the M1 and M2 sites. For the M2 site, it already started off low, at a 0.16 fraction for $x = 0$, which decreased to 0.069 for $x = 0.4$. However, for the M1 site a larger decrease is clearly visible, starting off at a 0.92 fraction for $x = 0$, and decreasing to a fraction of 0.765 for $x = 0.4$. Vanadium prefers to sit on the M1 site, likely due to its preference for tetrahedral coordination. However, the vanadium fully occupying the M2 site for $x = 0.1$ is rather odd, since this site is exclusively octahedrally coordinated. The decrease in the occupation of Mo/Nb on both the M1 and M2 sites is not interrupted by this, but the overall occupation is.
To verify whether vanadium truly prefers tetrahedral coordination and to clearly identify the reason as to why it sits at these sites, one would have to look at the oxygen sublattice. This cannot be done with XRD, and thus to confirm one would require the use of different analysis techniques, such as solid-state NMR and NPD. Especially the first, in the form of ^{51}V SS-NMR, can decipher the local coordination of vanadium from the average structure perspective, given by the XRD refinement data here.
With the XRD data we can only theorise on the implications. For instance, the localisation of vanadium on the M1 site for samples with $x > 0.1$, one would indeed expect an increase in the amount of tetrahedral coordination, which would increase the oxide ion conductivity. This trend has been seen in the work of Fop et al. [22], in terms of NPD by which the fraction of occupancy of the O3 increased, thereby implying an increase in tetrahedral coordination, with an increase in *x*. Here, more direct evidence is given, clearly showing occupation of vanadium on the only site that can coordinate tetrahedrally in the structure.

The second figure, figure 16, shows the change in the z-coordinate of the M1 site over the change in vanadium content. Despite the considerable uncertainty in the determination of the position of the average M1 site along the z-direction, changes observed among the samples of varying vanadium content are beyond the error margin from the refinement procedure, and are hence significant. With more vanadium, the z-coordinate first increases, after which it goes down to around its original position.
The initial slope upward could indeed be explained along the same reasoning as presented before in the LeBail refinement, in which the increase in vanadium causes an increase in tetrahedral coordination, thereby bringing the average z-coordinate of the M1 site above or below the palmierite plane. However, with the stretching of the unit cell in the *c*-direction with an increase in vanadium substitution, the z-coordinate of the M1 site could remain the same, for it is a fractional position. But since there is an observed change in the fractional z-coordinate, it would put favour to the hypothesis of either the elongation of the unit cell by an increase in second-order Jahn-Teller distortions or by repulsion between occupied O3 sites, thereby becoming the moving force behind the expansion of the unit cell in the *c*-direction.

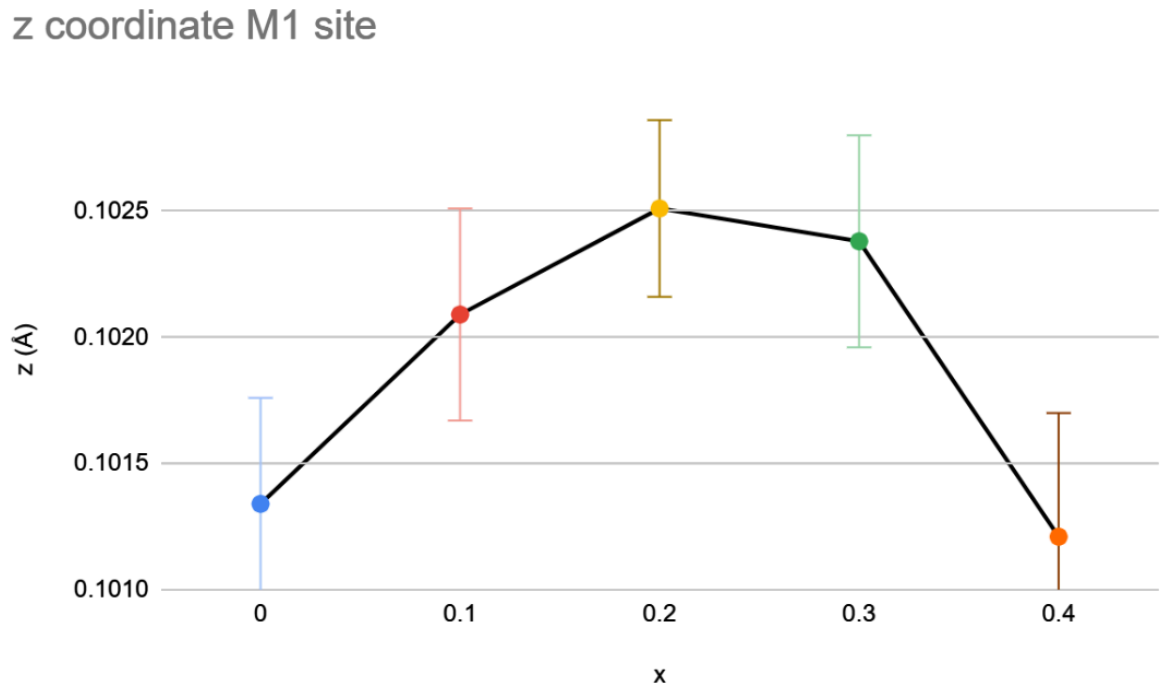

Figure 16. The average z-coordinate of the M1 site (Mo/Nb and V) from the Rietveld refinement of the XRD patterns for the $Ba_3MoNb_{1-x}V_xO_{8.5}$ samples, with x = 0.0, 0.1, 0.2, 0.3, and 0.4.

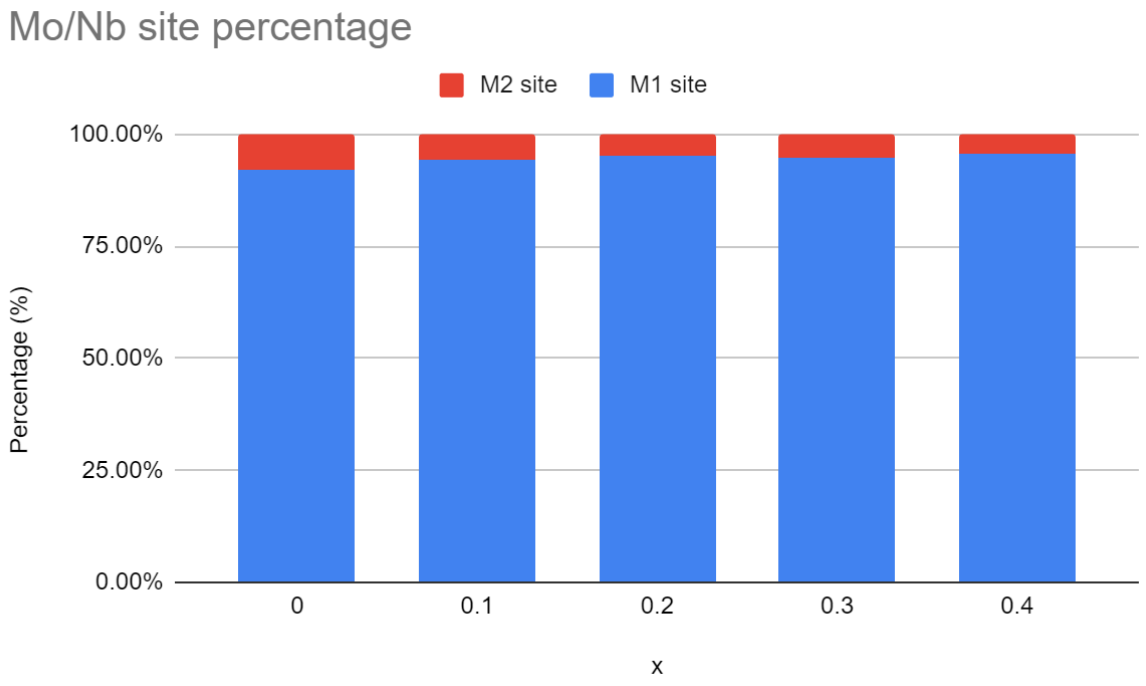

Figure 17. The percentages of the total Mo/Nb on the M1 site (blue) and the M2 site (red) from the Rietveld refinement of the XRD patterns for the $Ba_3MoNb_{1-x}V_xO_{8.5}$ samples, with x = 0.0, 0.1, 0.2, 0.3, and 0.4.

Finally, by taking into account the multiplicity of the sites, the total occupation of Mo/Nb on both the M1 and M2 sites were calculated, which has resulted in figure 17. Whilst the fractional occupancy in figure 13 showed a decrease of Mo/Nb on the M1 site, it did not take into account the multiplicity. There are twice the number of M1 sites than M2 sites per unit cell. Here it can be clearly seen that there is an increase in occupation on the M1 site and a decrease on the M2 site. The step from x = 0 to x = 0.1 is the largest with, which can be attributed to the preference of vanadium to sit on the M2 site. After vanadium moves to the M1 site, the movement of Mo/Nb towards the M1 site seems to cap off slightly.
This finding shows that even with vanadium preferring to occupy the M1 site, thereby filling a good portion of the sites, the molybdenum and niobium still move more towards the M1 site with an increase in substitution. This leaves the M2 site almost empty.
With vanadium sitting entirely on the M1 site from x = 0.2 onward, the M2 site is only marginally filled by molybdenum and niobium. From Gilane et al. [24] it was shown that a complete vacancy of the M2 site on $Ba_3WVO_{8.5}$ had led to a hindrance of long-range oxygen diffusion along the *c*-axis, which was subsequently hypothesised to be the explanation for its reduced ionic conductivity, compared to $Ba_3MoNbO_{8.5}$. Fop et al. [22] had already shown a reduced oxide ion conductivity for samples with a substitution of x = 0.2, 0.3, and 0.4. It could therefore be hypothesised that the decrease in occupation on the M2 site with an increase in vanadium substitution in our $Ba_3MoNb_{1-x}V_xO_{8.5}$ samples, could contribute to the decrease in ionic conductivity Fop had measured.

5. Conclusion.

In this thesis the synthesis method and the crystal structure of the $Ba_3MoNb_{1-x}V_xO_{8.5}$ series, with x = 0.0, 0.1, 0.2, 0.3, and 0.4, has been investigated. The synthesis for all samples was performed successfully by achieving phase pure samples, demonstrating the repeatability for this method. In doing so, there has also been a side investigation into the first calcination step. From this sidetrack, it has been concluded that with a higher calcination temperature and a longer calcination time, more of the desired end product forms, therefore giving no physical reason to perform this first step differently than other steps.

From the LeBail refinement the lattice parameters of each sample along the series were gathered, from which two separate trends were discovered; the *a* parameter follows along the lines of Vegard's law, in that it decreases with an increase in substitution of the relatively large Nb^{5+} ion for the relatively small V^{5+} ion. However, the *c* parameter follows an opposite manner, in which it increases upon the same increase of *x*. This is hypothesised to be due to the increased repulsion along the palmierite layers, either due to an increase in second-order Jahn-Teller distortion, and/or by an increase in tetrahedral coordination.

Finally, from the Rietveld refinement the occupation of the metallic cation sites was verified, in which the effect of vanadium was evidenced. It has shown that vanadium is incorporated into the solid solution and is preferably located on the tetrahedrally-coordinated M1 site, which is able to adapt either tetrahedral or octahedral coordination, in contrast to the exclusively octahedrally-coordinated M2 site. The only exception was found for the $Ba_3MoNb_{0.9}V_{0.1}O_{8.5}$, in which vanadium is located on the M2 site. Overall, a movement from the M2 to the M1 site is seen with an increase in vanadium content, thus showing that vanadium has an effect on the other metallic cations apart from its own localisation.

6. Outlook.

This thesis has given a brief look into the vast world of electrolytes in solid oxide fuel cells, in particular the $Ba_3M'M''O_{8.5}$ series. In choosing which metallic cations to pick, there has already been a good variety regarding secondary and even some tertiary structures and aliovalent doping using Mo^{6+}, Nb^{5+}, W^{6+}, and V^{6+}. However, many options and combinations are still left between these four, let alone the option to bring in other metallic cations in the mix, such as Cr^{6+} and Ta^{5+}. The opportunities are nearly endless, but to make an insightful hypothesis into what may and what may not work, more research is required into the structures that have already been synthesised.

Narrowing down the scope into the vanadium doped series investigated here, there are still many possibilities left to investigate its synthesis and structure. Whilst having provided good insight into lattice parameters and the location and occupancy of the metallic cations, XRD is clearly limited. As has been stated during the discussion as well, neutron powder diffraction could overcome some of its limitations, in the sense of being able to distinguish between Mo^{6+} and Nb^{5+}, as well as the ability to show the oxygen sublattice, thereby giving further understanding of the occupancy of both the metallic cation sites M1 and M2, and the oxygen sites. Taking this a step further, there is also the option to perform variable temperature NPD, thereby seeing how the occupancy of both the oxygen sublattice and the metallic cations differs over temperatures that would also be utilised during its use in a SOFC.

As stated, the manner in which the metallic cation can adapt lower coordination environments, such as tetrahedral polyhedra as opposed to octahedral polyhedra, is vital in

the way it conducts oxide ions. These coordination environments, their prevalence and orientation, can be identified using solid-state NMR. In particular, ^{51}V and ^{17}O SS-NMR would be of interest in the case of our $Ba_3MoNb_{1-x}V_xO_{8.5}$ samples, shining a light on how exactly vanadium is coordinating and in which manner that plays a role on the oxide ion conductivity. This could even be taken a step further, by applying variable temperature SS-NMR, giving a rise to the oxide ion conduction pathways.
The pathways can of course also be identified using BVSE analysis, by which the ionic migration along the structure is visualised. This would also highlight any energy barriers the oxide ions must overcome, and how they are influenced by the vanadium doping.
Finally, whilst not applying as much to the structural analysis, these compounds were made with the idea in mind for them to become electrolytes within a SOFC, and thus their oxide ion conductivity is of great importance to their eventual performance. This could be measured by electrochemical impedance spectroscopy, for which the compounds are required to be pelletised to an as high as feasible theoretical density. Under platinum coating, the oxide ion conductivity can then be measured accurately.
Overall, there is still much that can be done and discovered on this family of compounds, and many opportunities await in creating a solid electrolyte that will bring a revolution in the application of solid oxide fuel cells.

7. Acknowledgements.

Here I will express my gratitude to anyone that helped me during this project. First and foremost I would like to thank both my overseeing supervisor and my daily supervisor, Dr. Pedro Braga Groszewicz and Abdulkadir Olatunbosun Biffo. Their continued support, invaluable patience, and insightful feedback have made an immense impact on this work, and I could not have done it without them. I would also like to express my most sincere gratitude to the defence committee, especially Amarante J. Böttger for sharing her knowledge and expertise. Furthermore, I would like to acknowledge the time, support, and insight from any with whom I had the pleasure of working with at the TU Delft Reactor Institute. Finally, I would be remiss in not mentioning the support of my family and friends, especially from Marloes Schoone and Robert Bobbink for their everlasting moral and emotional support.

8. References.

[1] Kupecki, J., Motyliński, K., Skrzypkiewicz, M., Wierzbicki, M., & Naumovich, Y. (2017). Preliminary electrochemical characterization of anode supported solid oxide cell (As-soc) produced in the Institute of Power Engineering operated in electrolysis mode (Soec). *Archives of Thermodynamics*, *Vol. 38*(4), 53–63. https://doi.org/10.1515/aoter-2017-0024

[2] Xu, Q., Guo, Z., Xia, L., He, Q., Li, Z., Temitope Bello, I., Zheng, K., & Ni, M. (2022). A comprehensive review of solid oxide fuel cells operating on various promising alternative fuels. *Energy Conversion and Management*, *253*, 115175. https://doi.org/10.1016/j.enconman.2021.115175

[3] Mahato, N., Banerjee, A., Gupta, A., Omar, S., & Balani, K. (2015). Progress in material selection for solid oxide fuel cell technology: A review. Progress in Materials Science, 72, 141–337. https://doi.org/10.1016/j.pmatsci.2015.01.001

[4] Han, M., Tang, X., Yin, H., & Peng, S. (2007). Fabrication, microstructure and properties of a YSZ electrolyte for SOFCs. *Journal of Power Sources*, *165*(2), 757–763. https://doi.org/10.1016/j.jpowsour.2006.11.054

[5] Arifin, N. A., Afifi, A. A., Samreen, A., Hafriz, R. S. R. M., & Muchtar, A. (2023). Characteristic and challenges of scandia stabilized zirconia as solid oxide fuel cell material – In depth review. *Solid State Ionics*, *399*, 116302. https://doi.org/10.1016/j.ssi.2023.116302

[6] Sakurambo. (2007). Diagram of a solid oxide fuel cell. Own work, based on w:Image:Fcell_diagram_sofc.gif (public domain). https://commons.wikimedia.org/wiki/File:Solid_oxide_fuel_cell.svg

[7] Badwal, S. P. S., Fini, D., Ciacchi, F. T., Munnings, C., Kimpton, J. A., & Drennan, J. (2013). Structural and microstructural stability of ceria – gadolinia electrolyte exposed to reducing environments of high temperature fuel cells. Journal of Materials Chemistry A, 1(36), 10768–10782. https://doi.org/10.1039/C3TA11752A

[8] Wachsman, E. D., & Lee, K. T. (2011). Lowering the temperature of solid oxide fuel cells. Science, 334(6058), 935–939. https://doi.org/10.1126/science.1204090

[9] Lacorre, P., Goutenoire, F., Bohnke, O., Retoux, R., & Laligant, Y. (2000). Designing fast oxide-ion conductors based on La2Mo2O9. Nature, 404(6780), 856–858. https://doi.org/10.1038/35009069

[10] Srijith, Lakhanlal, Das, A., Dasari, H. P., & Saidutta, M. B. (2022). Electrical conductivity studies on LAMOX based electrolyte materials for solid oxide fuel cells. Ceramics International, 48(19, Part B), 29229–29237. https://doi.org/10.1016/j.ceramint.2022.05.198

[11] Abraham, F., Boivin, J. C., Mairesse, G., & Nowogrocki, G. (1990). The bimevox series: A new family of high performances oxide ion conductors. Solid State Ionics, 40–41, 934–937. https://doi.org/10.1016/0167-2738(90)90157-M

[12] Stroud, H. J., Mohn, C. E., Hernandez, J.-A., & Allan, N. L. (2021). Fast-ion conduction and local environments in BIMEVOX. Philosophical Transactions of the Royal Society A: Mathematical, Physical and Engineering Sciences, 379(2211), 20200430. https://doi.org/10.1098/rsta.2020.0430

[13] Ishihara, T., Matsuda, H., & Takita, Y. (1994). Doped lagao3 perovskite type oxide as a new oxide ionic conductor. Journal of the American Chemical Society, 116(9), 3801–3803. https://doi.org/10.1021/ja00088a016

[14] Feng, M., & Goodenough, J. B. (1995). Cheminform abstract: A superior oxide‐ion electrolyte. ChemInform, 26(7), chin.199507014. https://doi.org/10.1002/chin.199507014

[15] Yu, J., Liu, H., Chen, X., Xing, J., Yuan, B., Wang, M., & Ma, W. (2021). Ionic conductivity and crystal structure of LSGM with different element mole ratios. Fuel Cells, 21(2), 149–154. https://doi.org/10.1002/fuce.202000056

[16] Kuang, X., Allix, M., Ibberson, R. M., Claridge, J. B., Niu, H., & Rosseinsky, M. J. (2007). Oxygen Vacancy Ordering Phenomena in the Mixed-Conducting Hexagonal Perovskite Ba 7

Y 2 Mn 3 Ti 2 O 20. Chemistry of Materials, 19(11), 2884–2893. https://doi.org/10.1021/cm0626740

[17] Kanungo, S., Datta, R., Panda, S. K., & Saha-Dasgupta, T. (2013). Evolution of electronic and magnetic properties in four polytypes of BaRuO3: A first-principles study. Journal of Physics: Condensed Matter, 25(50), 505503. https://doi.org/10.1088/0953-8984/25/50/505503

[18] Fop, S., Skakle, J. M. S., McLaughlin, A. C., Connor, P. A., Irvine, J. T. S., Smith, R. I., & Wildman, E. J. (2016). Oxide Ion Conductivity in the Hexagonal Perovskite Derivative Ba3MoNbO8.5. Journal of the American Chemical Society, 138(51), 16764–16769. https://doi.org/10.1021/jacs.6b10730

[19] Fop, S., Wildman, E. J., Skakle, J. M. S., Ritter, C., & Mclaughlin, A. C. (2017). Electrical and Structural Characterization of Ba3Mo1-xNb1+xO8.5-x/2 : The Relationship between Mixed Coordination, Polyhedral Distortion and the Ionic Conductivity of Ba3MoNbO8.5. *Inorganic Chemistry*, *56*(17), 10505–10512. https://doi.org/10.1021/acs.inorgchem.7b01488

[20] McCombie, K. S., Wildman, E. J., Fop, S., Smith, R. I., Skakle, J. M. S., & Mclaughlin, A. C. (2018). The crystal structure and electrical properties of the oxide ion conductor Ba3WNbO8.5. *Journal of Materials Chemistry A*, *6*(13), 5290–5295. https://doi.org/10.1039/C7TA08989A

[21] Auckett, J. E., Milton, K. L., & Evans, I. R. (2019). Cation distributions and anion disorder in Ba3Nb*M*O8.5 (*M* = Mo, W) materials: Implications for oxide ion conductivity. *Chemistry of Materials*, *31*(5), 1715–1719. https://doi.org/10.1021/acs.chemmater.8b05179

[22] Fop, S., McCombie, K., Smith, R. I., & Mclaughlin, A. C. (2020). Enhanced Oxygen Ion Conductivity and Mechanistic Understanding in Ba3Nb1–xVxMoO8.5,. *Chemistry of Materials*, *32*(11), 4724–4733. https://doi.org/10.1021/acs.chemmater.0c01322

[23] Gilane, A., Fop, S., Sher, F., I. Smith, R., & C. Mclaughlin, A. (2020). The relationship between oxide-ion conductivity and cation vacancy order in the hybrid hexagonal perovskite Ba3VWO8.5. *Journal of Materials Chemistry A*, *8*(32), 16506–16514. https://doi.org/10.1039/D0TA05581F

[24] Gilane, A., Fop, S., Tawse, D. N., Ritter, C., & Mclaughlin, A. C. (2022). Variable temperature neutron diffraction study of the oxide ion conductor Ba3VWO8.5. *Inorganic Chemistry*, *61*(3), 1597–1602. https://doi.org/10.1021/acs.inorgchem.1c03354

[25] Kikuchi, Y., Yasui, Y., Hester, J. R., & Yashima, M. (2023). Improved oxide ion conductivity of hexagonal perovskite-related oxides Ba3W1+xV1−xO8.5+x/2. *Inorganics*, *11*(6), 238. https://doi.org/10.3390/inorganics11060238

[26] Tawse, D. N., Gilane, A., Fop, S., Martinez-Felipe, A., Sher, F., Smith, R. I., & Mclaughlin, A. C. (2021). Investigation of the Crystal Structure and Ionic Pathways of the Hexagonal Perovskite Derivative Ba3-xVMoO8.5-x. Inorganic Chemistry, 60(17), 13550–13556. https://doi.org/10.1021/acs.inorgchem.1c01840

[27] Assirey, E. A. R. (2019). Perovskite synthesis, properties and their related biochemical and industrial application. Saudi Pharmaceutical Journal, 27(6), 817–829. https://doi.org/10.1016/j.jsps.2019.05.003

[28] Woodward, P. M. (1997). Octahedral tilting in perovskites. I. Geometrical considerations. Acta Crystallographica Section B Structural Science, 53(1), 32–43. https://doi.org/10.1107/S0108768196010713

[29] Kajitani, M., Matsuda, M., Hoshikawa, A., Harjo, S., Kamiyama, T., Ishigaki, T., Izumi, F., & Miyake, M. (2005). In situ neutron diffraction study on fast oxide ion conductor LaGaO3-based perovskite compounds. Chemistry of Materials, 17(16), 4235–4243. https://doi.org/10.1021/cm050597n

[30] Fop, S., McCombie, K. S., Wildman, E. J., Skakle, J. M. S., & Mclaughlin, A. C. (2019). Hexagonal perovskite derivatives: A new direction in the design of oxide ion conducting materials. *Chemical Communications*, *55*(15), 2127–2137. https://doi.org/10.1039/C8CC09534E

[31] Kunz, M., & Brown, I. D. (1995). Out-of-center distortions around octahedrally coordinated d0 transition metals. Journal of Solid State Chemistry, 115(2), 395–406. https://doi.org/10.1006/jssc.1995.1150

[32] Gregors, L. png: U. work: (2011). Diagram of bragg's law angle of deviation 2 theta, interference can be constructive (Left) or destructive(Right). Loi_de_bragg.png. https://commons.wikimedia.org/wiki/File:Braggs_Law.svg
[33] Le Bail, A., Duroy, H., & Fourquet, J. L. (1988). Ab-initio structure determination of LiSbWO6 by X-ray powder diffraction. Materials Research Bulletin, 23(3), 447–452. https://doi.org/10.1016/0025-5408(88)90019-0
[34] Rietveld, H. M. (1969). A profile refinement method for nuclear and magnetic structures. Journal of Applied Crystallography, 2(2), 65–71. https://doi.org/10.1107/S0021889869006558
[35] Toby, B. H., & Von Dreele, R. B. (2013). "GSAS-II: the genesis of a modern open-source all purpose crystallography software package". Journal of Applied Crystallography, 46(2), 544-549. doi:10.1107/S0021889813003531
[36] Match! - Phase Analysis using Powder Diffraction, Crystal Impact - Dr. H. Putz & Dr. K. Brandenburg GbR, Kreuzherrenstr. 102, 53227 Bonn, Germany, https://www.crystalimpact.de/match.
[37] Templeton, L. K., & Pask, J. A. (1959). Formation of BaTiO 3 from BaCO 3 and TiO 2 in Air and in CO 2. Journal of the American Ceramic Society, 42(5), 212–216. https://doi.org/10.1111/j.1151-2916.1959.tb15455.x

Appendix.

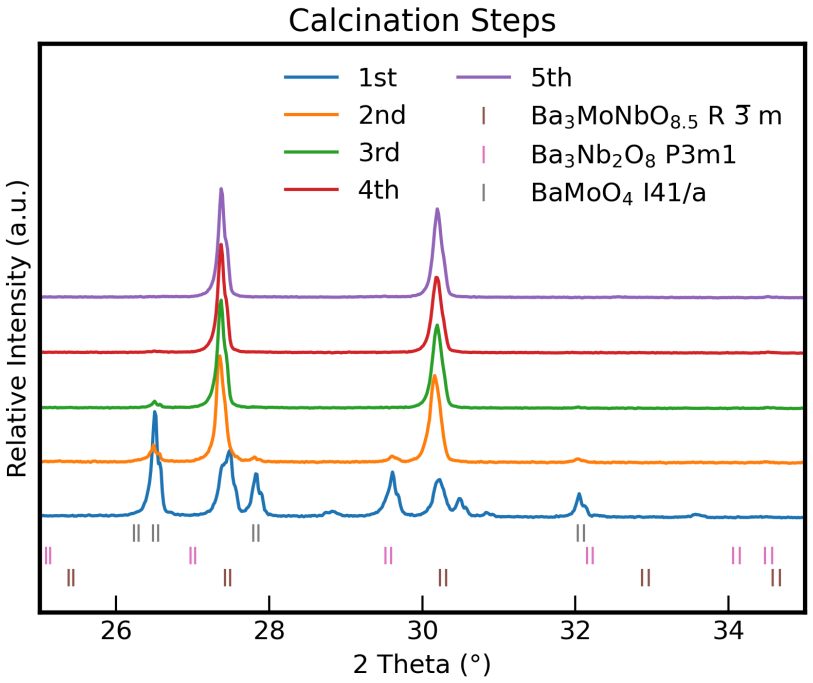

Appendix A1. Region from 25° to 35° 2θ of the XRD patterns of intermediate calcination steps for F001 sample. Matched phases displayed as vertical bars.

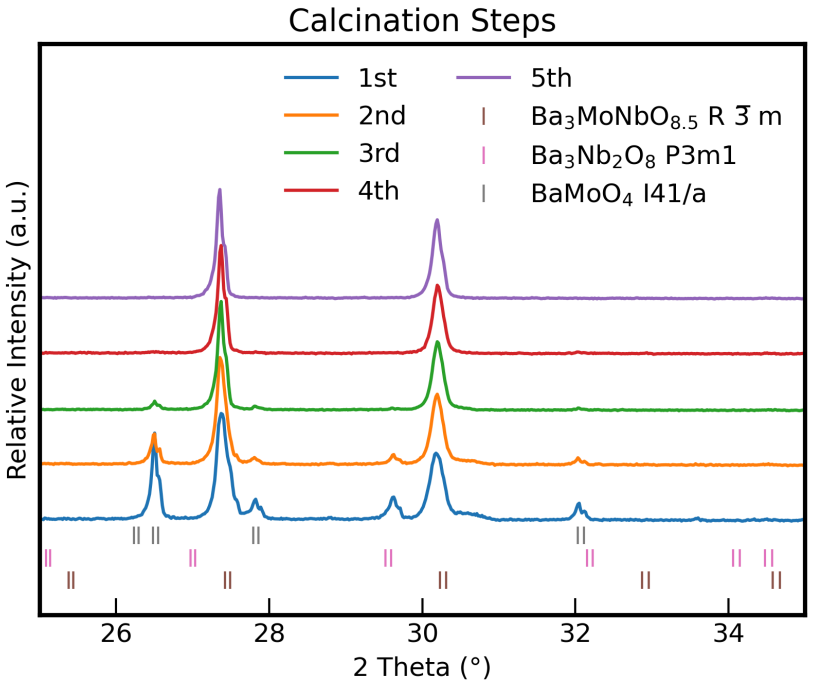

Appendix A2. Region from 25° to 35° 2θ of the XRD patterns of intermediate calcination steps for F003 sample. Matched phases displayed as vertical bars.

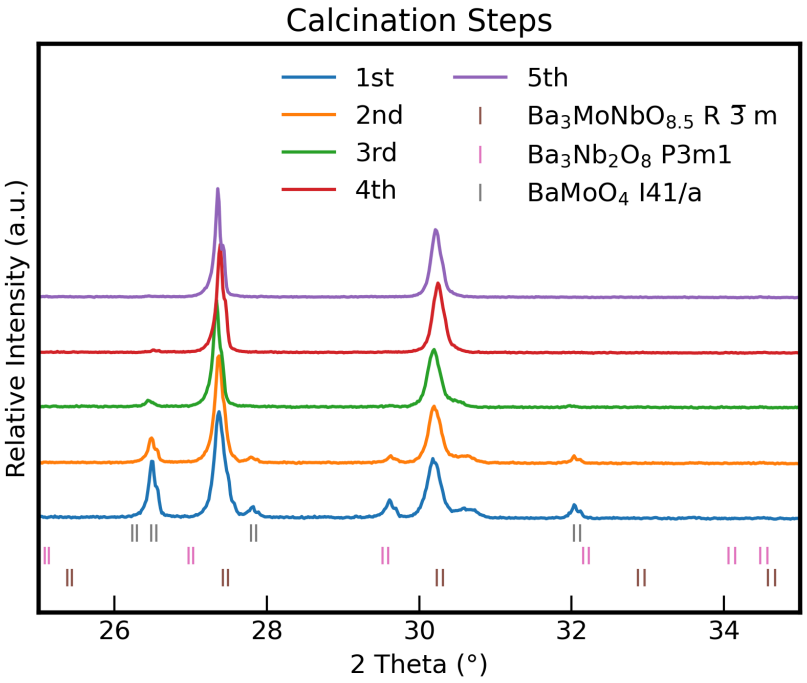

Appendix A3. Region from 25° to 35° 2θ of the XRD patterns of intermediate calcination steps for F004 sample. Matched phases displayed as vertical bars.

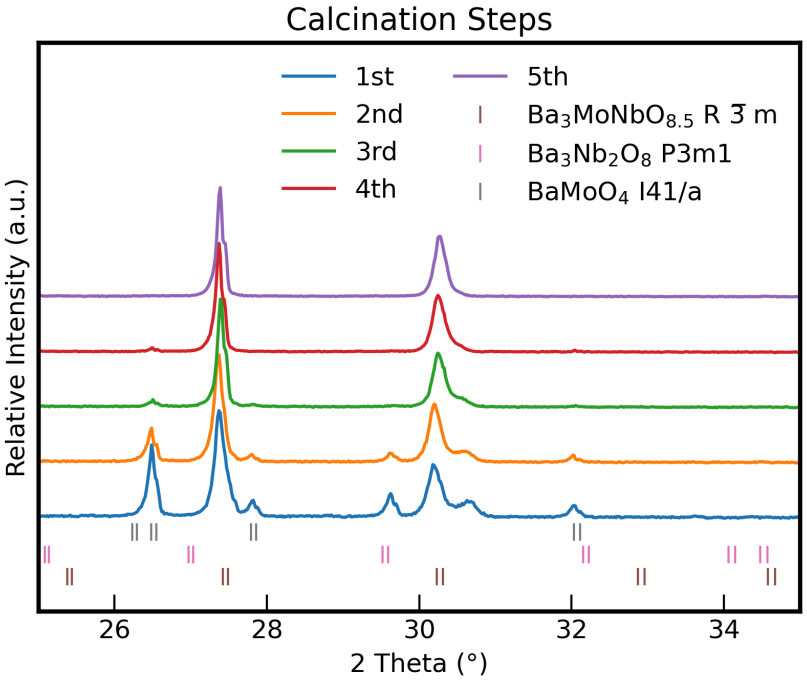

Appendix A4. Region from 25° to 35° 2θ of the XRD patterns of intermediate calcination steps for F005 sample. Matched phases displayed as vertical bars.

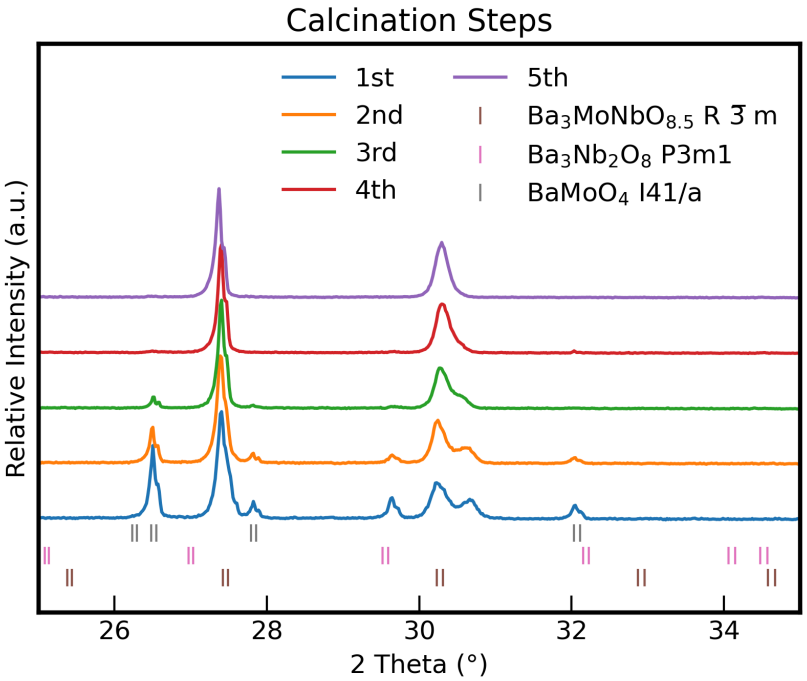

Appendix A5. Region from 25° to 35° 2θ of the XRD patterns of intermediate calcination steps for F006 sample. Matched phases displayed as vertical bars.

Phase Ba3 Mo Nb O8.5 from F001							
Space group = R -3 m							
a = 5.91515(17)							
b = 5.91515(17)							
c = 21.0794(4)							
alpha = 90							
beta = 90							
gamma = 120							
volume = 638.734(19)							
Atoms							
Label	Element	Multiplicity	x	y	z	Fraction	Uiso
Ba1	Ba	6	0.0000000	0.0000000	0.29145(23)	1.0000000	0.0150(12)
Ba2	Ba	3	0.0000000	0.0000000	0.5000000	1.0000000	0.0150(12)
Mo/Nb1	Nb	6	0.0000000	0.0000000	0.1013(4)	0.920(4)	0.0071(23)
Mo/Nb2	Nb	3	0.0000000	0.0000000	0.0000000	0.160(9)	0.0071(23)
O1	O	36	0.0930000	0.0080000	0.1800000	0.0900000	0.0127000
O2	O	18	0.5070000	0.4930000	0.2700000	1.0000000	0.0127000
O3	O	9	0.5000000	0.0000000	0.5000000	0.4700000	0.0127000
wR = 11.806							
GOF = 2.67							
reduced chi**2 = 7.15							

Appendix A6. Refined atomic parameters from Rietveld fit of the X-ray diffraction data of $Ba_3MoNbO_{8.5}$ (F001).

.

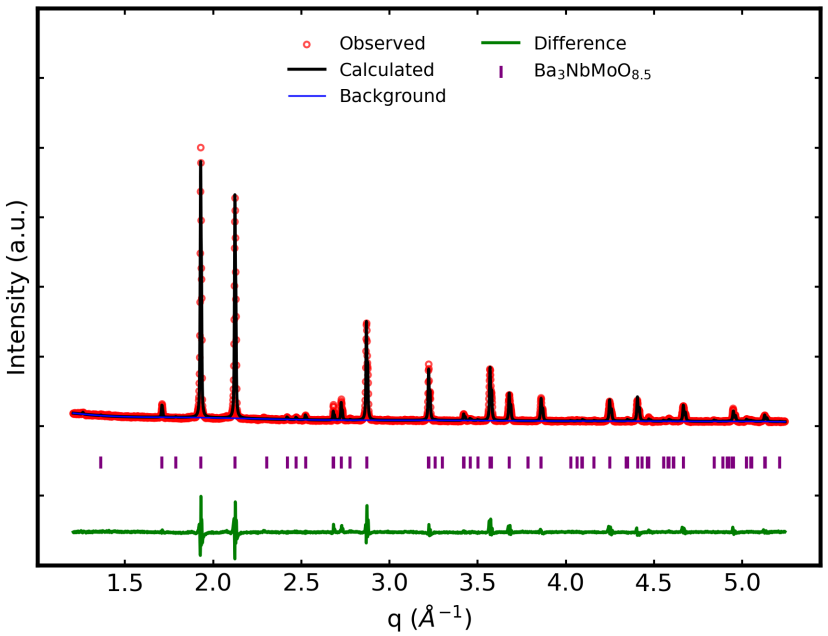

Appendix A7. Rietveld fit to the structural model of $Ba_3MoNbO_{8.5}$ (F001) from X-ray diffraction data.

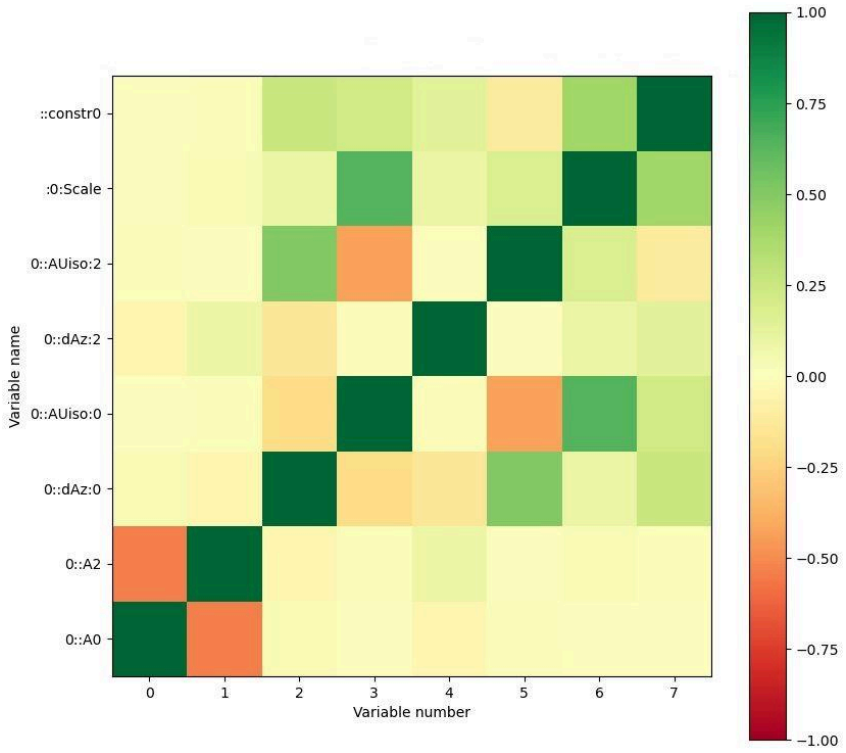

Appendix A8. Covariance matrix of the Rietveld refinement of the structural model of $Ba_3MoNbO_{8.5}$ (F001) from X-ray diffraction data. The variables on the y-axis are denoted '0::' to indicate $Ba_3MoNb_{0.8}V_{0.2}O_{8.5}$. The variables on the y-axis are the lattice parameters (a = A0 & c = A2), the z coordinates of the atoms (barium = dAz:0 & metallic cations = dAz:2), the U_{iso} of the atoms (barium = AUiso:0 & metallic cations = AUiso:2), the scale of the compound (Scale), and the constraints applied (constr0)

Phase Ba3 Mo Nb O8.5 from F003							
Space group = R -3 m							
a = 5.91245(16)							
b = 5.91245(16)							
c = 21.0916(4)							
alpha = 90							
beta = 90							
gamma = 120							
volume = 638.519(18)							
Atoms							
Label	Element	Multiplicity	x	y	z	Fraction	Uiso
Ba1	Ba	6	0.0000000	0.0000000	0.2927760	1.0000000	0.0035(8)
Ba2	Ba	3	0.0000000	0.0000000	0.5000000	1.0000000	0.0035(8)
Mo/Nb1	Nb	6	0.0000000	0.0000000	0.1030(3)	0.894(4)	0.0302(19)
Mo/Nb2	Nb	3	0.0000000	0.0000000	0.0000000	0.112(8)	0.0302(19)
V2	V	3	0.0000000	0.0000000	0.0000000	0.1000000	0.0302(19)
O1	O	36	0.0930000	0.0080000	0.1800000	0.0900000	0.0127000
O2	O	18	0.5070000	0.4930000	0.2700000	1.0000000	0.0127000
O3	O	9	0.5000000	0.0000000	0.5000000	0.4700000	0.0127000
wR = 11.673							
GOF = 3.91							
reduced chi**2 = 15.27							

Appendix A9. Refined atomic parameters from Rietveld fit of the X-ray diffraction data of $Ba_3MoNb_{0.9}V_{0.1}O_{8.5}$ (F003).

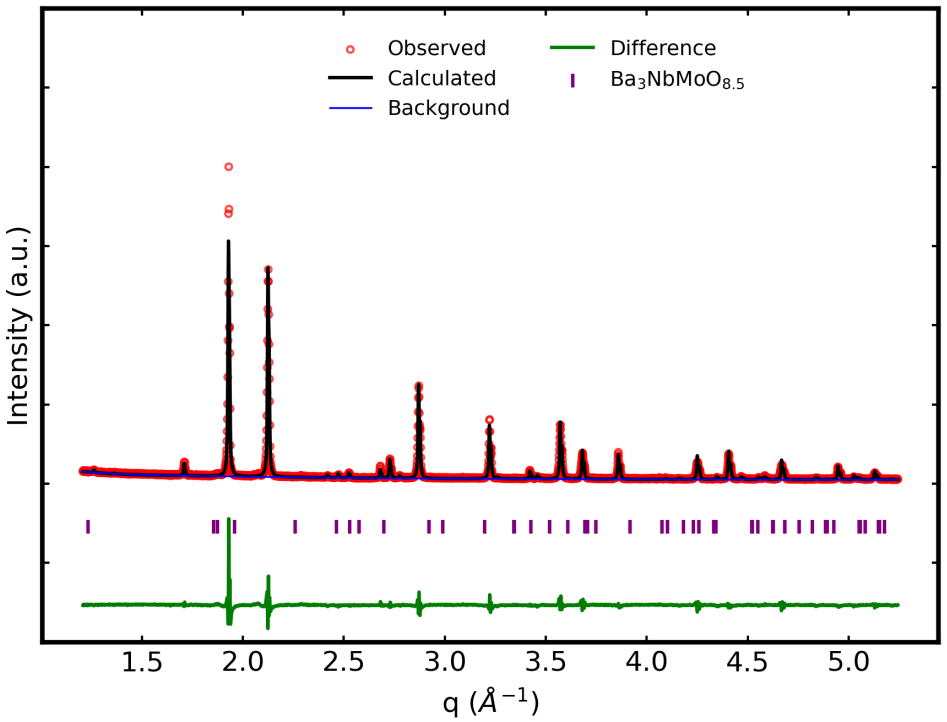

Appendix A10. Rietveld fit to the structural model of $Ba_3MoNb_{0.9}V_{0.1}O_{8.5}$ (F003) from X-ray diffraction data.

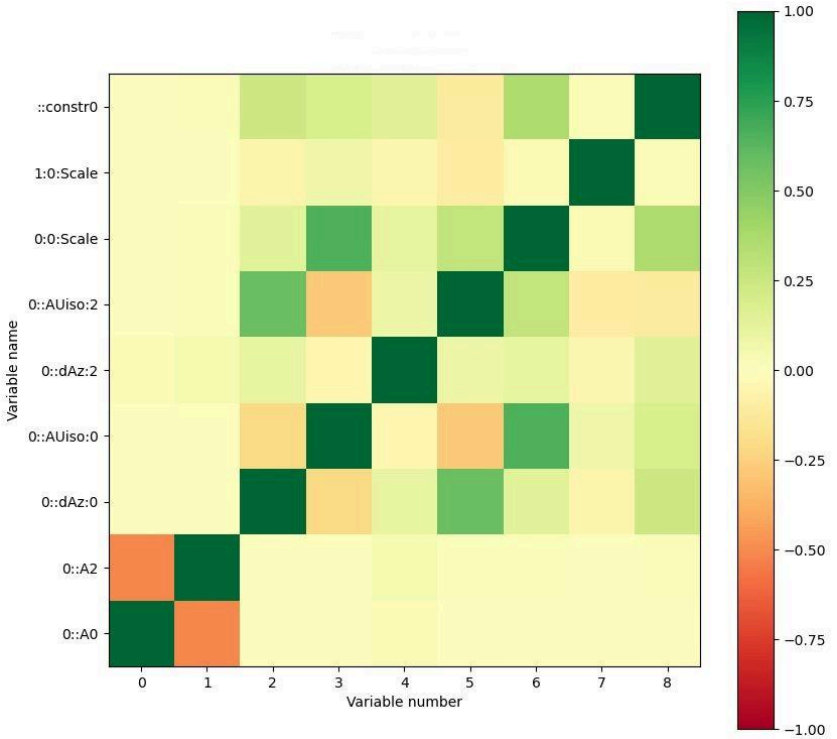

Appendix A11. Covariance matrix of the Rietveld refinement of the structural model of $Ba_3MoNb_{0.9}V_{0.1}O_{8.5}$ (F003) from X-ray diffraction data. The variables on the y-axis are denoted '0::' to indicate $Ba_3MoNb_{0.9}V_{0.1}O_{8.5}$ and 1:: to indicate $BaMoO_4$. The variables on the y-axis are the lattice parameters (a = A0 & c = A2), the z coordinates of the atoms (barium = dAz:0 & metallic cations = dAz:2), the U_{iso} of the atoms (barium = AUiso:0 & metallic cations = AUiso:2), the scale of the compound (Scale), and the constraints applied (constr0)

Phase Ba3 Mo Nb O8.5 from F004							
Space group = R -3 m							
a = 5.90589(18)							
b = 5.90589(18)							
c = 21.0980(5)							
alpha = 90							
beta = 90							
gamma = 120							
volume = 637.300(20)							
Atoms							
Label	Element	Multiplicity	x	y	z	Fraction	Uiso
Ba1	Ba	6	0.0000000	0.0000000	0.29070(19)	1.0000000	0.0053(9)
Ba2	Ba	3	0.0000000	0.0000000	0.5000000	1.0000000	0.0053(9)
V1	V	6	0.0000000	0.0000000	0.1025(3)	0.1000000	0.0074(20)
Mo/Nb1	Nb	6	0.0000000	0.0000000	0.1025(3)	0.857(4)	0.0074(20)
Mo/Nb2	Nb	3	0.0000000	0.0000000	0.0000000	0.087(7)	0.0074(20)
O1	O	36	0.0930000	0.0080000	0.1800000	0.0900000	0.0127000
O2	O	18	0.5070000	0.4930000	0.2700000	1.0000000	0.0127000
O3	O	9	0.5000000	0.0000000	0.5000000	0.4700000	0.0127000
wR = 9.481							
GOF = 3.4							
reduced chi**2 = 11.58							

Appendix A12. Refined atomic parameters from Rietveld fit of the X-ray diffraction data of $Ba_3MoNb_{0.8}V_{0.2}O_{8.5}$ (F004).

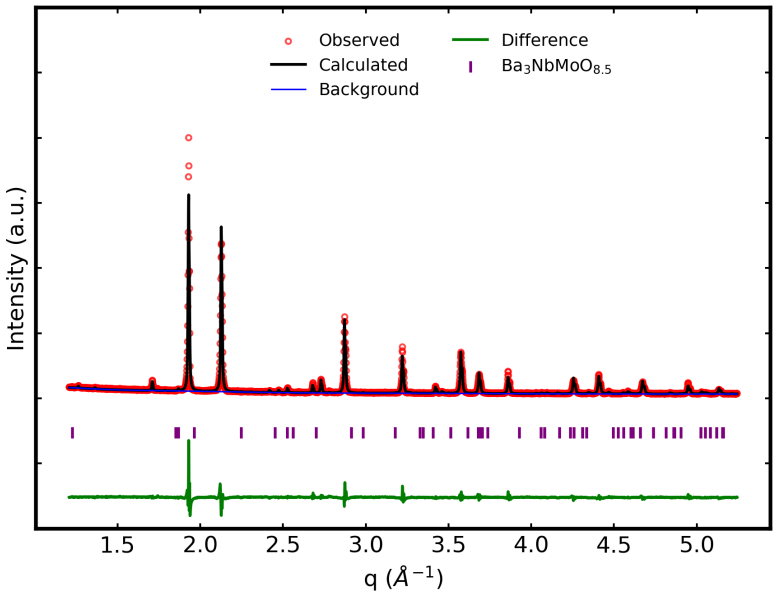

Appendix A13. Rietveld fit to the structural model of $Ba_3MoNb_{0.8}V_{0.2}O_{8.5}$ (F004) from X-ray diffraction data.

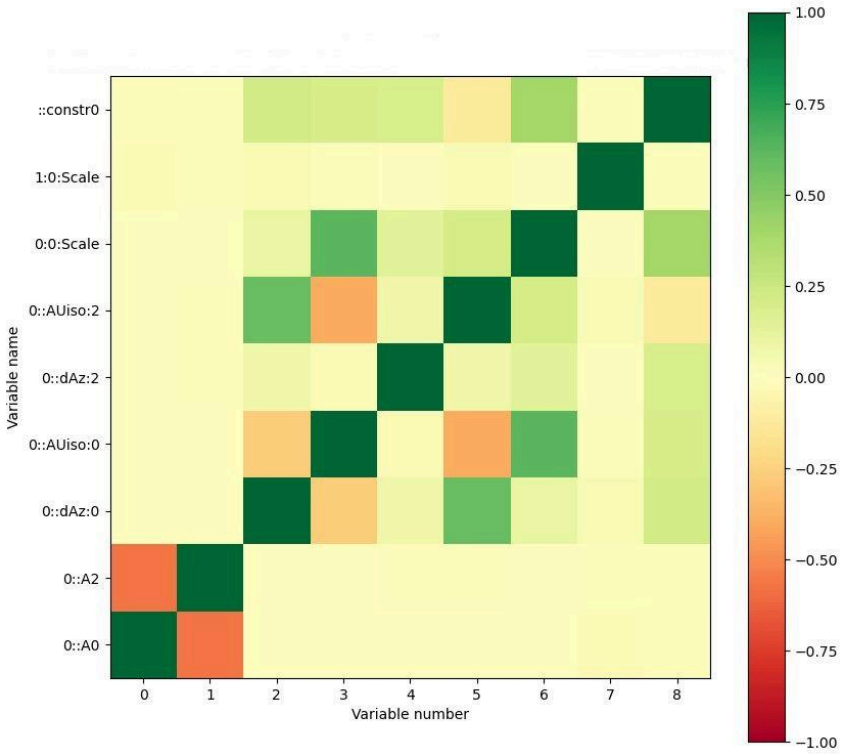

Appendix A14. Covariance matrix of the Rietveld refinement of the structural model of $Ba_3MoNb_{0.8}V_{0.2}O_{8.5}$ (F004) from X-ray diffraction data. The variables on the y-axis are denoted '0::' to indicate $Ba_3MoNb_{0.8}V_{0.2}O_{8.5}$ and 1:: to indicate $BaMoO_4$. The variables on the y-axis are the lattice parameters (a = A0 & c = A2), the z coordinates of the atoms (barium = dAz:0 & metallic cations = dAz:2), the U_{iso} of the atoms (barium = AUiso:0 & metallic cations = AUiso:2), the scale of the compound (Scale), and the constraints applied (constr0)

Phase Ba3 Mo Nb O8.5 from F005							
Space group = R -3 m							
a = 5.89906(19)							
b = 5.89906(19)							
c = 21.1074(5)							
alpha = 90							
beta = 90							
gamma = 120							
volume = 636.110(21)							
Atoms							
Label	Element	Multiplicity	x	y	z	Fraction	Uiso
Ba1	Ba	6	0.0000000	0.0000000	0.29157(24)	1.0000000	0.0143(11)
Ba2	Ba	3	0.0000000	0.0000000	0.5000000	1.0000000	0.0143(11)
V1	V	6	0.0000000	0.0000000	0.1024(4)	0.1500000	0.0144(25)
Mo/Nb1	Nb	6	0.0000000	0.0000000	0.1024(4)	0.806(5)	0.0144(25)
Mo/Nb2	Nb	3	0.0000000	0.0000000	0.0000000	0.087(9)	0.0144(25)
O1	O	36	0.0930000	0.0080000	0.1800000	0.0900000	0.0127000
O2	O	18	0.5070000	0.4930000	0.2700000	1.0000000	0.0127000
O3	O	9	0.5000000	0.0000000	0.5000000	0.4700000	0.0127000
wR = 13.007							
GOF = 4.32							
reduced chi**2 = 18.63							

Appendix A15. Refined atomic parameters from Rietveld fit of the X-ray diffraction data of $Ba_3MoNb_{0.7}V_{0.3}O_{8.5}$ (F005).

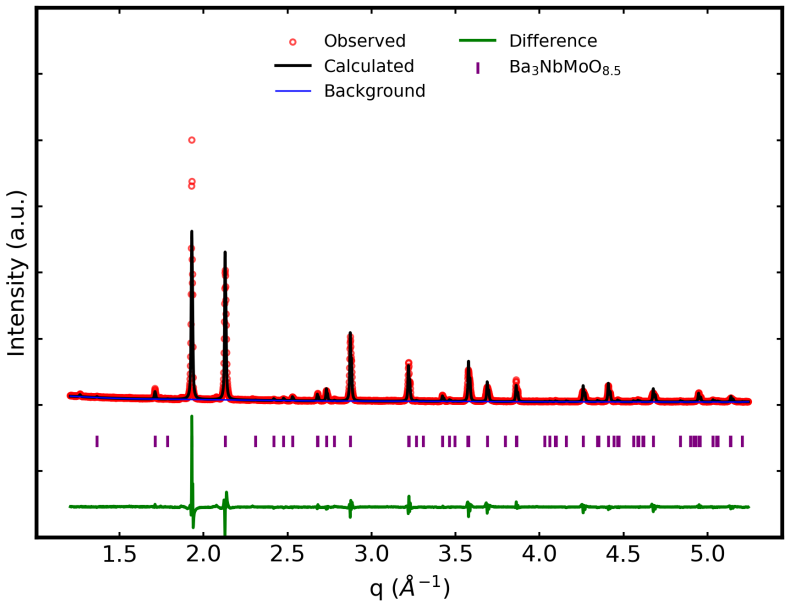

Appendix A16. Rietveld fit to the structural model of $Ba_3MoNb_{0.7}V_{0.3}O_{8.5}$ (F005) from X-ray diffraction data.

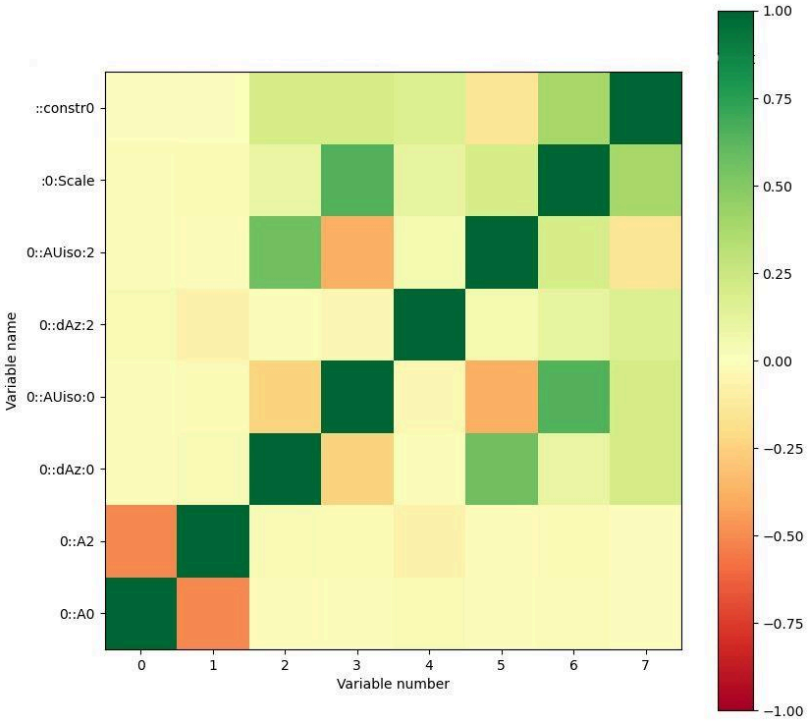

Appendix A17. Covariance matrix of the Rietveld refinement of the structural model of $Ba_3MoNb_{0.7}V_{0.3}O_{8.5}$ (F005) from X-ray diffraction data. The variables on the y-axis are denoted '0::' to indicate $Ba_3MoNb_{0.7}V_{0.3}O_{8.5}$. The variables on the y-axis are the lattice parameters (a = A0 & c = A2), the z coordinates of the atoms (barium = dAz:0 & metallic cations = dAz:2), the U_{iso} of the atoms (barium = AUiso:0 & metallic cations = AUiso:2), the scale of the compound (Scale), and the constraints applied (constr0)

Phase Ba3 Mo Nb O8.5 from F006							
Space group = R -3 m							
a = 5.88970(26)							
b = 5.88970(26)							
c = 21.1069(6)							
alpha = 90							
beta = 90							
gamma = 120							
volume = 634.078(28)							
Atoms							
Label	Element	Multiplicity	x	y	z	Fraction	Uiso
Ba1	Ba	6	0.0000000	0.0000000	0.29181(26)	1.0000000	0.0142(11)
Ba2	Ba	3	0.0000000	0.0000000	0.5000000	1.0000000	0.0142(11)
V1	V	6	0.0000000	0.0000000	0.1012(5)	0.2000000	0.0114(26)
Mo/Nb1	Nb	6	0.0000000	0.0000000	0.1012(5)	0.765(5)	0.0114(26)
Mo/Nb2	Nb	3	0.0000000	0.0000000	0.0000000	0.069(9)	0.0114(26)
O1	O	36	0.0930000	0.0080000	0.1800000	0.0900000	0.0127000
O2	O	18	0.5070000	0.4930000	0.2700000	1.0000000	0.0127000
O3	O	9	0.5000000	0.0000000	0.5000000	0.4700000	0.0127000
wR = 12.765							
GOF = 4.17							
reduced chi**2 = 17.38							

Appendix 18. Refined atomic parameters from Rietveld fit of the X-ray diffraction data of $Ba_3MoNb_{0.6}V_{0.4}O_{8.5}$ (F006).

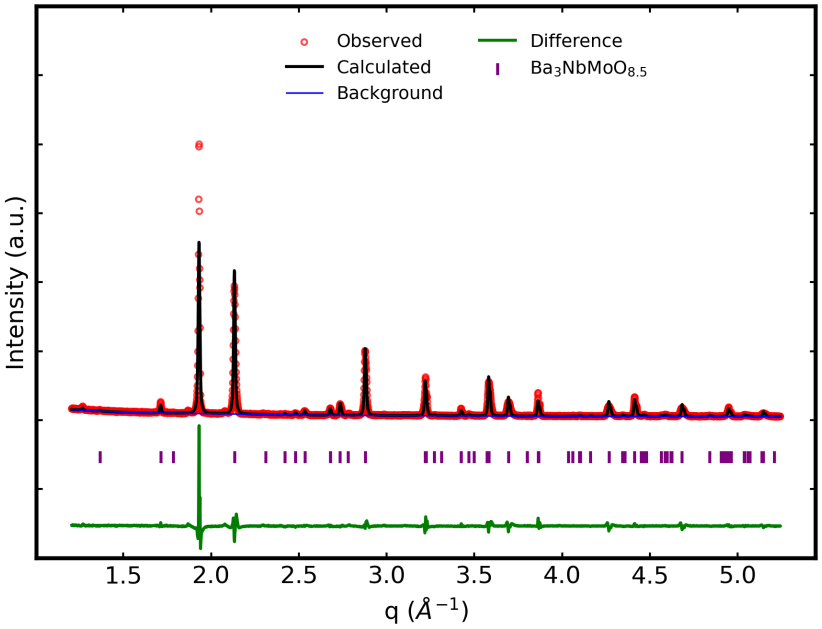

Appendix A19. Rietveld fit to the structural model of $Ba_3MoNb_{0.6}V_{0.4}O_{8.5}$ (F006) from X-ray diffraction data.

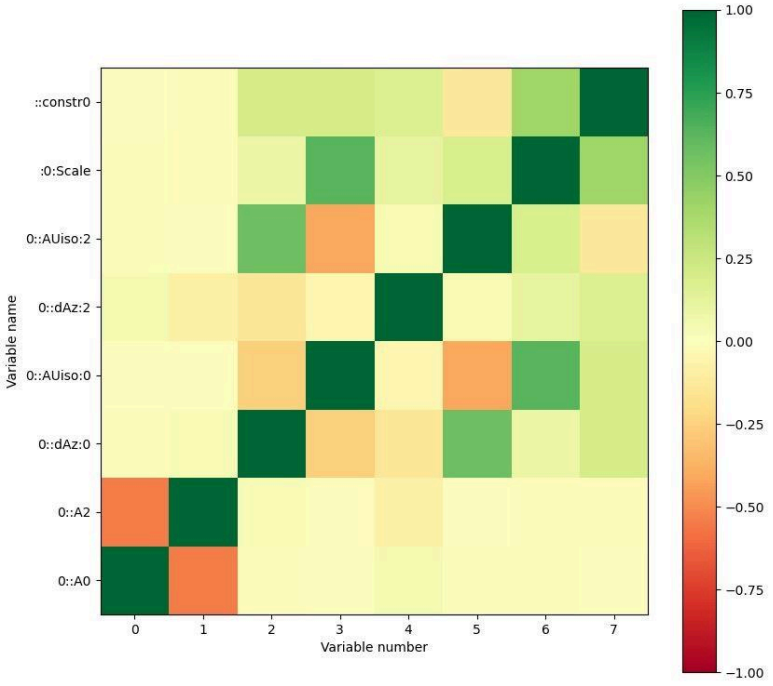

Appendix A20. Covariance matrix of the Rietveld refinement of the structural model of $Ba_3MoNb_{0.6}V_{0.4}O_{8.5}$ (F006) from X-ray diffraction data. The variables on the y-axis are denoted '0::' to indicate $Ba_3MoNb_{0.6}V_{0.4}O_{8.5}$. The variables on the y-axis are the lattice parameters (a = A0 & c = A2), the z coordinates of the atoms (barium = dAz:0 & metallic cations = dAz:2), the U_{iso} of the atoms (barium = AUiso:0 & metallic cations = AUiso:2), the scale of the compound (Scale), and the constraints applied (constr0)